

Geochemistry, Geophysics, Geosystems

RESEARCH ARTICLE

10.1029/2020GC009431

Key Points:

- At least three Caribbean segments subduct under South America, one detached under the Mérida Andes. Detachment due to lithospheric weakness
- Post-break recoupling and rollback of slab contribute to uplift of Mérida Andes
- Northern subduction boundary identified

Supporting Information:

Supporting Information may be found in the online version of this article.

Correspondence to:

J. Cornthwaite,
jpcorn@rice.edu

Citation:

Cornthwaite, J., Bezada, M. J., Miao, W., Schmitz, M., Prieto, G. A., Dionicio, V., et al. (2021). Caribbean slab segmentation beneath northwest South America revealed by 3-D finite frequency teleseismic P-wave tomography. *Geochemistry, Geophysics, Geosystems*, 22, e2020GC009431. <https://doi.org/10.1029/2020GC009431>

Received 11 SEP 2020
 Accepted 10 MAR 2021

Caribbean Slab Segmentation Beneath Northwest South America Revealed by 3-D Finite Frequency Teleseismic P-Wave Tomography

John Cornthwaite¹ , Maximiliano J. Bezada² , Wenpei Miao¹ , Michael Schmitz³ , Germán A. Prieto⁴ , Viviana Dionicio⁵, Fenglin Niu¹ , and Alan Levander¹ 

¹Department of Earth, Environmental and Planetary Sciences, Rice University, Houston, TX, USA, ²Department of Earth and Environmental Sciences, University of Minnesota, Minneapolis, MN, USA, ³Fundación Venezolana de Investigaciones Sismológicas (FUNVISIS), Caracas, Venezuela, ⁴Department de Geociencias Universidad Nacional de Colombia, Bogotá, Colombia, ⁵Servicio Geológico Colombiano, Bogotá, Colombia

Abstract The Caribbean plate subducts beneath northwest South America at a shallow angle due to a large igneous province that added up to 12 km of buoyant crust. The overriding plate lacks volcanism and exhibits Laramide-style uplifts over 500 km from the trench. Here, we illuminate the subduction structures through finite frequency teleseismic P-wave tomography and connect those structures to the Laramide-style deformation on the overriding plate. We use a new data set collected from the Caribbean-Mérida Andes seismic experiment comprised of 65 temporary broadband stations integrated with permanent stations from the Colombian and Venezuelan national networks. We identify three segments of subducting Caribbean plate with one segment completely detached from the surface. The timing of the detachment aligns with other regional events, including the uplift of the Mérida Andes, about 10 Ma. Slab buoyancy post-detachment likely resulted in recoupling with the overriding plate, reactivation of Jurassic-aged rift structures and subsequent uplift of the Mérida Andes. Mantle counterflow over the broken segment induced by rollback of the attached slab likely contributed to the uplift of the Mérida Andes. We conclude that the northern limit of subduction lies south of the Oca-Ancón fault, though the fault itself may be the surface expression of the boundary. The southern limit of subduction lies south of our study area.

Plain Language Summary At the convergent boundary between the southern Caribbean and northwest South America the Caribbean plate dips, or subducts, beneath South America at angles less than 30° for up to ~300 km inland before steepening. Such low-angle subduction systems are unique because they produce mountains hundreds of kilometers inland. Using new data collected by the Caribbean-Mérida Andes seismic array, which continuously recorded earthquakes for two years, we imaged the Caribbean plate to depths of 660 km and identified at least three segments, including a segment detached from the surface. The timing of the detachment ~5–15 million years ago aligns with the uplift of the Mérida Andes of Venezuela ~500 km inland. Both the attached and detached segments interacted with the underside of South America, compressing parts of it, and causing uplift of the Mérida Andes. The northern limit of subduction lies south of the Oca-Ancón fault of northern Colombia and Venezuela. The southern expanse of subduction includes the Bucaramanga earthquake cluster, but the boundary lies south of our study area. By understanding how the actively subducting plate, the Caribbean, deforms the upper plate, South America, we can better assess seismic risk and understand similar systems that are no longer active.

1. Introduction

Flat slab subduction generally refers to slabs that extend nearly horizontally for some distance, sometimes hundreds of kilometers, in the upper mantle (Cahill & Isacks, 1992). We distinguish flat subduction from under-thrusting by noting that an under-thrusted slab remains in contact with the overriding plate and no asthenosphere material separates them (Pennington, 1981). Flat slab subduction zones comprise about 10% of all subduction zones and have several features in common, including: (1) Increased upper plate seismicity compared to steep subduction (Gutscher et al., 2000); (2) Orogenesis hundreds of kilometers from the

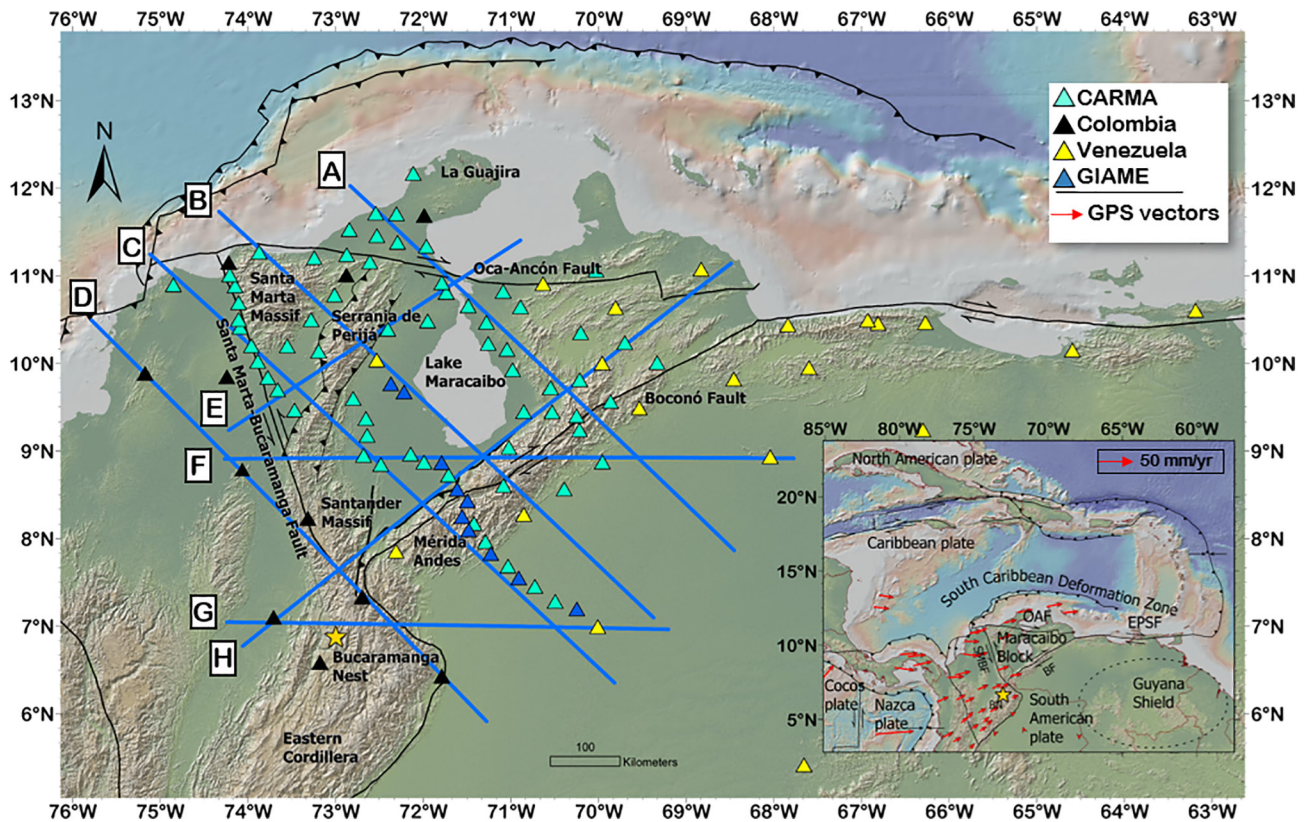


Figure 1. Geographic locations of the CARMArray and permanent stations used in teleseismic tomography and the local tomography used in crustal model. Labeled blue lines trace the profiles in Figure 6. BF: Boconó fault; OAF: Oca-Ancón fault; SMBF: Santa Marta-Bucaramanga fault; BN: Bucaramanga nest; MA: Mérida Andes; SdP: Serranía de Perijá; SMM: Santa Marta Massif; SM: Santander Massif. GPS data from Mora-Páez et al. (2019).

trench (Bird, 1988; Humphreys et al., 2003; Jordan & Allmendinger, 1986); (3) Volcanism that is either atypically far from the trench or absent altogether (e.g., Bishop et al., 2017; Eakin et al., 2014; Kay et al., 1987). The southernmost edge of the Caribbean (CAR) plate subducts obliquely at a low angle beneath northwestern South America (NWSA) due to a buoyant large igneous province impinging on a trench that lies offshore northwestern Colombia (Figure 1) (Burke, 1988; Kellogg & Bonini, 1982; Pennington, 1981). Like other flat slab subduction zones, the overriding South American plate has lacked magmatism for at least 45 m.y., has mountains up to ~500 km from the trench and is seismically active over that same length (Figures 3 and S1) (e.g., Cardona, Valencia, Bayona, et al., 2011; Mora et al., 2017; Taboada et al., 2000). However, the subducting CAR has not been previously well imaged due to limited instrumentation, leaving open questions regarding how the flat slab contributes to the Laramide-style uplifts seen in NWSA (e.g., Audemard & Audemard, 2002; Monod et al., 2010).

Laramide-style uplifts are characterized by basement-involved foreland deformation giving rise to basement-cored mountains (Brown et al., 1988; Fan & Carrapa, 2014; Jordan & Allmendinger, 1986; Smithson et al., 1978). The commonly proposed mechanisms that led to the Laramide uplifts of the western US include the low-angle subduction of the Shatsky rise conjugate on the Farallon plate (Bird, 1988; English & Johnston, 2010; Fan & Carrapa, 2014; Humphreys et al., 2003; Liu et al., 2010). Some models invoke direct transfer of stress from the Farallon to the North American plate through mechanisms such as interplate coupling (Bird, 1988; Saleeby, 2003) or bulldozing of material (Axen et al., 2018; McQuarrie & Chase, 2000). Other models invoke dynamic response due to mantle upwelling as the slab retreats or sinks (Humphreys et al., 2003; Liu et al., 2010). Despite being well-studied, the often-referenced Laramide orogeny is still poorly understood in part because it is no longer an active subduction zone.

The basement-involved thrust systems that formed the SdP and MA are thought to be analogous to the thrust systems that formed the Rocky Mountains during the Laramide orogeny (De Toni & Kellogg, 1993;

Duerto et al., 2006; Kellogg & Bonini, 1982). Like the Laramide, extended plate coupling due to flat subduction of the CLIP is one mechanism proposed to have driven the uplift of the MA (Duerto et al., 2006). Additional proposals include continental subduction (Chacín et al., 2005; Colletta et al., 1997) or an orogenic float (Audemard & Audemard, 2002; Cediel et al., 2003) whereby the MA are detached from the lithosphere and uplifted via distant stresses that are transferred from near the trench. Thus, the precise mechanism for the formation of the MA remains uncertain (Audemard & Audemard, 2002; English & Johnston, 2010; Erslev, 2005; Monod et al., 2010).

In addition to the question of the CAR's role in mountain building, the basic question of the geometry of the subducting CAR remains open. From north to south, the Caribbean plate starts as sea floor before under-thrusting beneath northern Colombia and Venezuela. In northern Colombia, the CAR transitions from under-thrusting to subducting beneath NWSA. Where this transition occurs is not resolved. It has been proposed to be along the Oca-Ancón fault near Lake Maracaibo (Masy et al., 2015) and south of the Oca-Ancón fault near the Santa Marta Massif (Mora et al., 2017). Farther south the subduction of CAR ends. Not only is the location of this boundary unclear, with various authors proposing a boundary between 5°N–9°N, but identifying the location is complicated by other slabs, notably the Nazca slab, possibly overlapping with the CAR (e.g., Chiarabba et al., 2015; Idárraga-García et al., 2016; Kellogg et al., 2019; Malavé & Suárez, 1995; Sanchez-Rojas & Palma, 2014; Syracuse et al., 2016; Taboada et al., 2000).

In this study, we use finite-frequency teleseismic P-wave tomography to resolve structures in the CAR-NWSA subduction zone and suggest how the flat subduction has mechanically resulted in the formation of Laramide-style uplifts in the Serranía de Perijá and Mérida Andes. The data were recorded by a 65-element portable broadband seismograph network deployed in NWSA and 39 broadband stations of the Venezuelan and Colombian national seismograph networks. We constrain the geometry and timing of the subduction system by identifying and mapping slab segments and using subduction rates by previous authors to deduce the subduction history of the CAR. We then compare the subduction history to the tectonic history of NWSA to hypothesize the role of the CAR.

1.1. Tectonic Background

In the hot spot reference frame, the CAR has remained roughly fixed at a constant longitude since 55 Ma as the Americas moved westward (Boschman et al., 2014; Jordan, 1975; Pindell et al., 1998). Along the Southern Caribbean Deformation Belt, where no physiographic trench is visible due to sedimentation into the Colombia and Venezuela basins, the CAR under-thrusts the northern edge of NWSA and subducts beneath the northwest margin of NWSA (Figure 1) (Miller et al., 2009; van der Hilst & Mann, 1994). The CAR began subducting beneath NWSA between 70 and 55 Ma, coinciding with magmatism along the margin (Cardona, Valencia, Bayona, et al., 2011; Mora et al., 2017). By 45–55 Ma magmatism abruptly ceased, likely due to the onset of low-angle subduction of the Caribbean Large Igneous Province (CLIP) (Montes et al., 2019; Mora et al., 2017; Taboada et al., 2000). The CLIP is thought to have been erupted from the Galapagos hot spot in the late Cretaceous and added 12 or more kilometers of buoyant crust atop the oceanic plate (Kerr et al., 1997). Since 45 Ma the CAR-NWSA subduction zone has lacked volcanism and seen uplift of the Santa Marta Massif (SMM), the Serranía de Perijá (SdP), and the Mérida Andes (MA)—the latter being ~500 km from the trench (Figure 1) (Kellogg & Bonini, 1982). Both the SdP and the MA were primarily uplifted since ~10 Ma (Bermudez et al., 2010; Cediel et al., 2003; Kellogg & Bonini, 1982).

NWSA is seismically active due to deformation in both the overriding and subducting plate (Figures 3 and S1). Plate boundary deformation is accommodated by slip on the Boconó fault, Santa Marta-Bucaramanga fault, as well as the El Pilar-San Sebastian fault system and several other secondary faults (Figure 1). The El Pilar-San Sebastian fault accommodates nearly all the CAR-SA strike-slip motion (Symithe et al., 2015). The Boconó fault accommodates 9–11 mm/yr of dextral shear and 1 mm/yr of compression (Kellogg & Bonini, 1982). The Santa Marta-Bucaramanga fault accommodates about 6 mm/yr of left-lateral slip (Symithe et al., 2015). The Oca-Ancón fault (OAF) and the many secondary faults slip at a rate of 2 mm/yr or less (Audemard & Audemard, 2002). Together, these three fault systems facilitate the escape of the Maracaibo Block (MB) over the CAR (Figure 1). Most seismicity in western Venezuela occurs shallower than 30 km (Malavé & Suárez, 1995), but Benioff seismicity is observed beneath the SdP and Santander Massif (Figures 3 and S1).

1.2. Previous Work

Several previous studies proposed geometries of the subducting CAR. As in the flat slab segments of western South America (e.g., Antonijevic et al., 2015; Bishop et al., 2017; Cahill & Isacks, 1992; Gutscher, Malavielle, et al., 1999; Gutscher, Olivet, et al., 1999; Jordan & Allmendinger, 1986; Ramos & Folguera, 2009), the CAR slab subducts with a shallow angle at shallow depths, then transitions to a much steeper angle some distance inland. Early studies used hypocenters to determine the shallow slab dipped from $\sim 15^\circ$ to 30° at an azimuth of 109° to a depth of 200 km beneath the Maracaibo basin (Kellogg & Bonini, 1982; Pennington, 1981). From tomography van der Hilst and Mann (1994) estimated the slab dipped at $17^\circ \pm 3^\circ$ in a direction of $150^\circ \pm 20^\circ$. They also interpreted an overlap between two slabs at the Bucaramanga seismic cluster. Subsequent studies measured the flat segment dip at $\sim 25^\circ$ (Malavé & Suárez, 1995; Ojeda & Havskov, 2001; Zarifi et al., 2007) to as much as 40° (van Benthem et al., 2013). Bernal-Olaya et al. (2015) found that the slab varied from north (as little as 8°) to south (as much as 35°). The steeply dipping segment was imaged to the 660 discontinuity beneath the MA by Bezada et al. (2010) and van Benthem et al. (2013) and was interpreted to penetrate the 660 by Taboada et al. (2000).

In some subduction zones the subducting plate is separated from nonsubducting plate by lithospheric tearing at a Subduction-Transform Edge Propagator (STEP) fault (Govers & Wortel, 2005). North of SA the CAR comprises the sea floor and, in some locations, under-thrusts SA to depths of ~ 150 km (Guedez et al., 2007; Masy et al., 2015; Sanchez et al., 2010; Schmitz et al., 2008; Van der Hilst & Mann, 1994). To accommodate the transition between where it is under-thrusting seafloor and where it is deeply subducting there must be a tear or major deformation of the plate. The northern edge of the CAR-NWSA subduction system has not been identified, so it is not clear whether a STEP fault accommodates a transition between subducting and nonsubducting/under-thrusting CAR or if subduction is continuous along the entirety of the NWSA margin. Authors have proposed both continuous deforming CAR (e.g., Sanchez et al., 2010; van der Hilst & Mann, 1994) and subducting/nonsubducting CAR separated by a tear (Masy et al., 2011; Mora et al., 2017; Taboada et al., 2000). CAR under-thrusting from the north has been partially imaged in several studies of varying resolution (Guedez et al., 2007; Masy et al., 2015; Miller et al., 2009; Sanchez et al., 2010; Schmitz et al., 2008).

The southern boundary of the subducting CAR slab is poorly defined. It has been interpreted as a continuous plate to at least as far south as the Caldas tear at 5°N (Cortes & Angelier, 2005; Kellogg et al., 2019; Pennington, 1981; Van der Hilst & Mann, 1994; Vargas & Mann, 2013; Yarce et al., 2014) or only as far south as the Bucaramanga seismic nest at 7°N (Figure 1) (Chiarabba et al., 2015; Idárraga-García et al., 2016; Sanchez-Rojas & Palma, 2014; Syracuse et al., 2016). At Bucaramanga, the relationship between the seismic cluster and plate configurations is also poorly understood. Some authors have interpreted the cluster as indicative of a boundary between two slabs (Sanchez-Rojas & Palma, 2014; Syracuse et al., 2016; Zarifi et al., 2007) while others see the cluster origin wholly within the Nazca plate (Chiarabba et al., 2015; Van der Hilst & Mann, 1994) or wholly within the Caribbean plate (Cortes & Angelier, 2005; Kellogg et al., 2019; Pennington, 1981; Taboada et al., 2000; Vargas & Mann, 2013; Yarce et al., 2014). Thus, the southern boundary of the Caribbean slab might not be a clear delineation, but rather a confluence of overlapping and interacting slabs that may include the Nazca plate or some other intermediate slab segment.

2. Data and Methods

2.1. Data

Data were collected during the CARibbean-Mérida Andes seismic experiment (CARMArray) (Levander, 2016) which comprised 65 IRIS-PASSCAL broadband (BB) stations deployed from April 2016 to March 2018, with 19 BB stations from the permanent Venezuela National Seismic Network, 12 stations from the GIAME project in Venezuela, and 8 BB stations from the permanent Colombian National Seismic Network (Table S1). Combined, the arrays extend from the Caribbean coast of northwest Colombia to 200 km east of the Mérida Andes and along the Venezuelan coast, with station spacing of ~ 40 – 75 km (Figure 1). Embedded in the layout are two dense lines with ~ 20 km station spacing that extend from the Colombian coast to the Mérida Andes in the northern and southern edges of the study area.

Our Vp tomography used 148 events with Mb \geq 5.5 and epicentral distances of 30°–95° (113 events) and 150°–180° (35 events) (Figure 2). Waveforms were bandpass filtered into three narrow frequency bands centered at 1.0, 0.5, and 0.3 Hz. Relative traveltimes for P and PKIKP phases were computed by cross-correlating the waveforms (VanDecar & Crosson, 1990) so that each waveform had a delay for each frequency band. The delays were then demeaned for each event. Waveforms that had delays greater than 3 s were discarded. After running the inversion several iterations, residuals were inspected. Waveforms with residuals greater than 5 standard deviations above the mean were removed, leaving a total of 23,675 teleseismic P-delays used in the inversion with 7,833 from the 1.0 Hz band, 7,948 from the 0.5 Hz band and 7,894 from the 0.3 Hz band.

2.2. Finite Frequency Teleseismic Tomography

We used nonlinear 3-D finite-frequency teleseismic P-wave tomography code of Schmandt and Humphreys (2010) as modified by Bezada et al. (2013) and the details of the method are found therein. Here we provide details of our setup. Our model domain is $\sim 2,150 \times 1,550$ km and centered at 8.8°N, 69.2°W. The grid size varies both laterally and vertically with lateral grid spacing varying from 42 km within the footprint of our array to 56 km outside of the array and vertical spacing increasing from 35 to 55 km with increasing depth. The vertical spacing of the upper 90 km varied from 5 to 10 km. The code uses an iterative solver and computes 1-D travel times using the AK135 Earth model (Kennett et al., 1995) from event source to the model domain, so-called source-to-box times, and the Stingray 3-D ray tracer (Hammond & Toomey, 2003; Toomey et al., 1994) to compute traveltimes from the edge of the domain through the model volume to the stations. Approximate Born sensitivity kernels were calculated after each iteration. Various damping and smoothing regularizations were tested to balance data variance reduction with model variance reduction (Figure S6). Values of 2 and 10 were chosen for damping and smoothing, respectively. Limited results for additional parameters are in Supplementary Information (Figure S7). We ran the code 6 iterations, which maximized variance reduction and minimized data misfit (Figure S8). Total variance was reduced by $\sim 91.5\%$ and the final rms data misfit was 0.195 s.

2.3. Inclusion of Shallow Structure in Tomography

To address unconstrained shallow layers and prevent unimaged shallow structure from being mapped to deeper parts of the model we created a 3-D local P-wave tomography model and inserted the upper 80 km of it into the upper 80 km of the starting teleseismic tomography model (Figures S1–S5). Details of the crustal model may be found in supporting information. The mean velocity at each depth was removed to produce anomalies compatible with the teleseismic tomography inversion. The local tomography used 1,369 local earthquakes with depths of 5–200 km and stations with predicted (based on the AK135 model) traveltimes residuals less than 2 s (Kennett et al., 1995). Since the local tomography model is smaller in extent than the teleseismic model, values were extrapolated by the nearest-neighbor algorithm.

2.4. Model Resolvability

To understand our model resolvability, we utilize two tools—ray hit count quality and synthetic tomography. Hit quality is calculated as the weighted average of number of rays present in each of six 60° azimuthal bins at each node. Bins saturate at six rays so that a score of one means that at least six rays were present in every bin for a node. For each node the scores of the six bins were averaged to provide the final hit count quality. We consider values above 0.6 to be well-resolved. Areas with hit quality less than 0.6 and 0.3 are shaded light gray and dark gray, respectively (Figure 4).

Using the event-station geometry of our data set we created synthetic tomographic images to evaluate the details of the velocity model (Figures 3 and 7). We performed a checkboard test and two image recovery tests by creating slab structures within our model domain characterized by large fast anomalies. For the checkerboard test, we created synthetic traveltimes through a checkerboard velocity model and completed the inversion with the unconstrained upper 60 km highly damped. The checkerboard test reveals that within the footprint of the CARMArray $\pm 5\%$ velocity anomalies can be expected to be recovered as ± 2 – 4% anomalies, but outside of the footprint anomalies will not be well recovered (Figures 3a–3g). The test

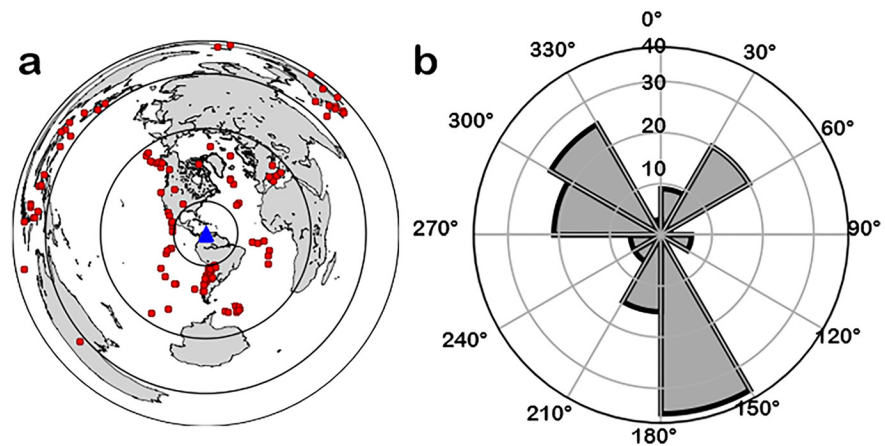


Figure 2. Events used in the teleseismic tomography. (a) Teleseismic events. (b) Back-azimuth distribution of teleseismic events.

also revealed that lateral smearing is minimal but there is some vertical smearing, particularly toward the south-southeast where the largest concentration of events originates.

The first recovery test is a southeast-dipping continuous slab with a +5% anomaly that extends across the study area (Figures 3h and 3i). The inversion used identical damping and smoothing as the model. Like the checkerboard test, it shows that the slab-like anomaly is recovered within the footprint of the array. Velocity perturbations of 1%–2% are recovered at 125 km, but larger amplitudes are recovered at greater depth. There is some vertical smearing between 200 and 300 km and weak slow anomalies appear that were not part of the input. At 390 km depth there is a small break in the anomaly at its southern limit, which cautions against interpreting diverging plates at that depth in the model. The second recovery test is derived directly from the tomography: We created three surfaces from the fast anomalies and converted contours of those surfaces back into synthetic 5% fast anomalies (Figure S9). We ran two versions of this test: one with three slabs and the other with two slabs. We will discuss the second recovery test in the results section in the context of our tomographic images, as they provide us with a qualitative proxy for model resolution and robustness in our final tomographic model.

Overall, resolution is strongest within the footprint of the array. The southern edge of the study area, south of 7° near Bucaramanga, is complicated and not likely well resolved above 200 km or below 500 km. For shallow structure we use seismicity to improve our interpretations. The synthetic tests indicate that smearing, though present, does not obscure the imaged structures. We confine our interpretations to areas with a hit quality greater than 0.6.

3. Results

Here, we describe our tomographic model and compare it to the synthetic model described previously to determine the structure of the deeper subduction system. We observe three fast anomalies continuous through several depths, two of which connect at shallow depths but separate as depth increases. The third anomaly starts at ~200 km under the MA and appears to merge with another of the anomalies at greater depth. We also observe two fast anomalies identified only at depths less than 195 km at the northern and southern edges of the model.

Shown in Figure 4 are map views of the subduction system starting at 60 km depth down to 635 km depth. In each panel the anomaly label orientations are meant to match the strike of the anomalies. The fast anomalies at depths of 60–90 km under the SMM might be the flat portion of the Caribbean plate. The down-going Caribbean plate is the prominent fast (1%–3%), continuous feature at 125 km (labeled S1, for subduction) and follows the seismicity along the SdP and Santa Marta-Bucaramanga fault. The strike of S1 is concave at shallow depths but becomes more linear with increasing depth (Figures 4 and 5). From 125 to 195 km the S1 strike roughly parallels the Santander Massif and the SdP. Our synthetic image (Figure 7)

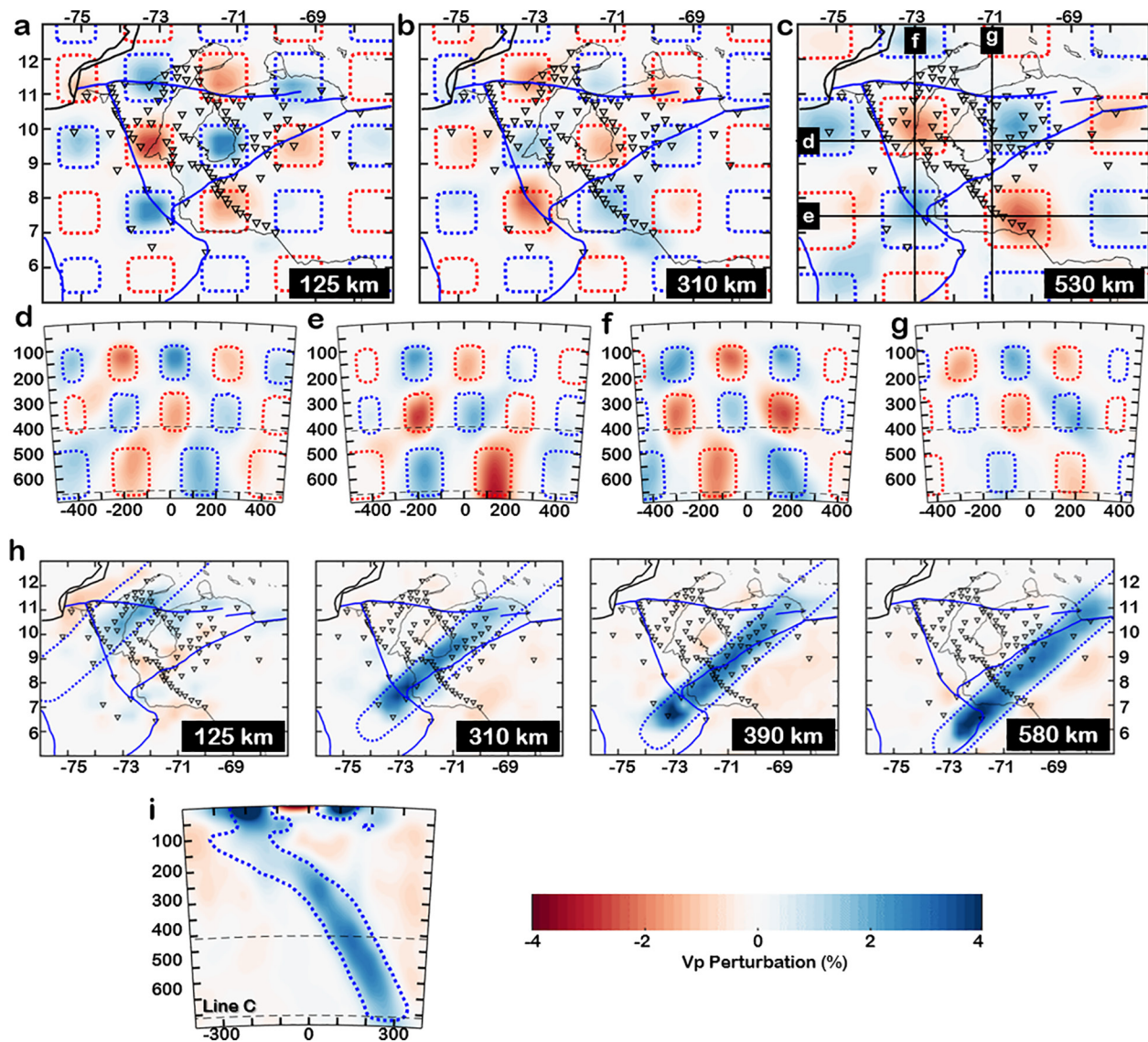


Figure 3. (a–g) Telesismic tomography checkerboard test with three layers. Input anomalies (dashed red and blue lines) are $\pm 5\%$ against the background model. (h) Synthetic test with a single, southeast-dipping 5% fast anomaly. A shallow depth slice and three depths where S1 and S3 interact the most. No anomalous structures appear in the recovered synthetic images. (i) Profile taken along line C where the S1/S3 anomaly is most identifiable in the model.

shows that this geometry is recovered except at the southwestern corner of the SdP. Also notable is that S1 extends to just south of the OAF where it connects to another anomaly, U (for under-thrust), that strikes mostly east-west (4). Segment U is not clearly identifiable deeper than 195 km. To the south at 125 km depth is a fast anomaly, S2, that we partition into shallow S2a and deeper S2b. The strikes of S2a and S2b also differ as S2a is generally north-south while S2b is northeast-southwest. S2 starts ~ 300 km farther inland than S1 and maintain strikes distinct from S1. From 195–435 km depth S1 exhibits nearly constant slope from the SdP to the MA (Figure 6). Another anomaly, S3, appears under the MA at ~ 160 km depth and merges with S1 by ~ 400 km depth. East of the MA S3 dips steeply, nearly reaching the bottom of the MTZ where the model domain ends. At 310 km depth S2b and S3 anomalies appear continuous, but their strikes are clearly different.

In our synthetic image at 195 km we inserted an anomaly corresponding to S3 (Figure 7). We do not see vertical smearing of that anomaly. Also, when S3 is not included in the synthetic no fast anomalies appear in its place. At 350 km depth we model S1 and S3 with as little as 40 km of separation. As in the tomography,

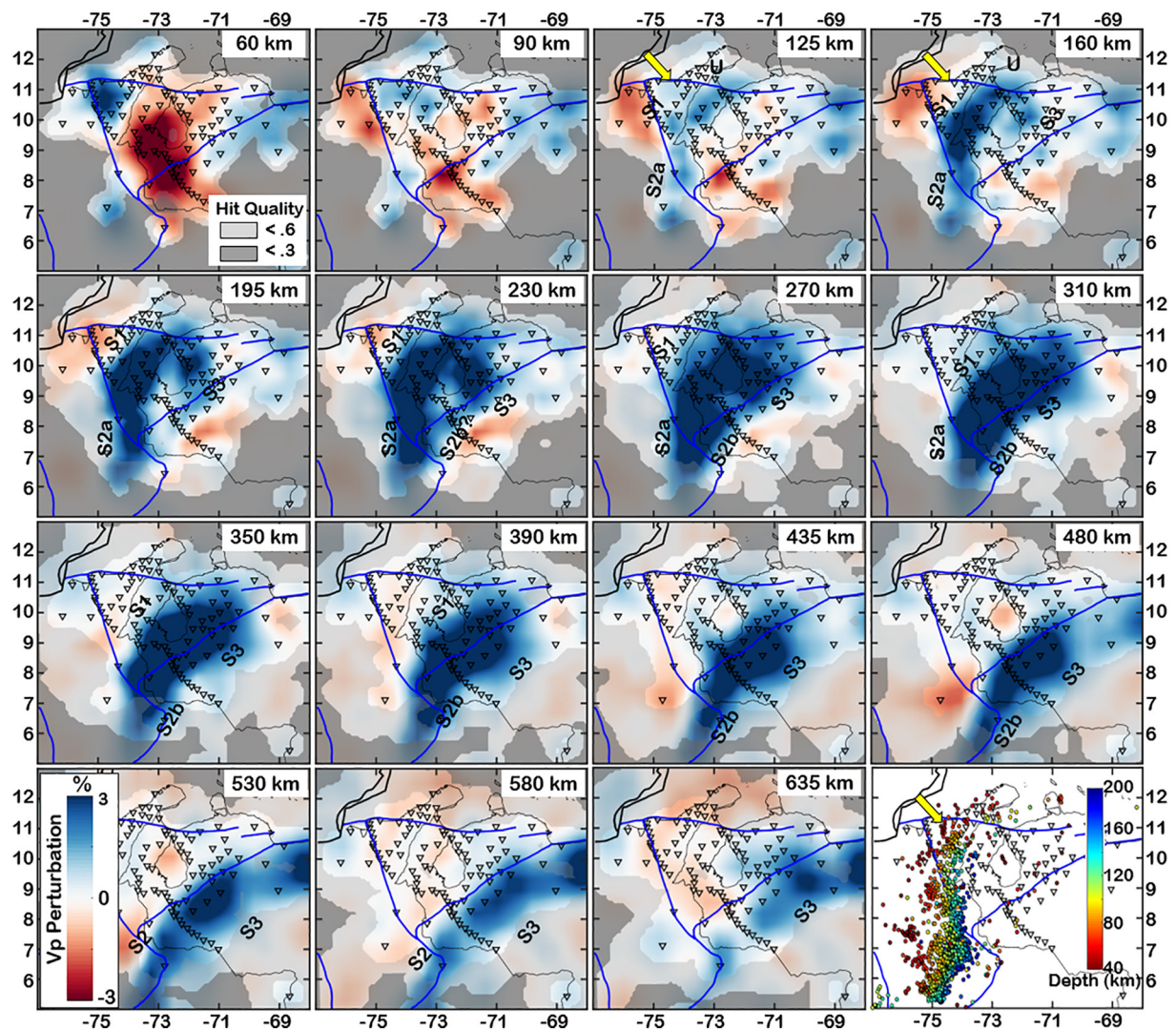


Figure 4. Map view of the model at 15 depths. The CAR anomaly moves from northwest to southeast with depth. Triangles: CARMArray stations. Yellow arrow: Location where intermediate depth seismicity ends. Events from Servicio Geológico Colombiano catalog, January 2000-February 2018 (Servicio Geológico Colombiano, 2020), and the ISC earthquake catalog, January 2010-January 2016 (International Seismological Centre, 2020).

the synthetic image demonstrates the two anomalies are distinguishable. At 435 km depth S1 has nearly completely merged with S3. At that depth S2 and S3 appear continuous in our model with slightly different strikes. We placed a gap between them in our synthetic, and what results are two distinct anomalies, unlike in the tomography model.

Profiles A-D (Figure 6) are roughly perpendicular to the MA and are sub-perpendicular to the SdP. They extend in the dip direction across the SdP and show the slab from ~80 to 690 km depth. In profiles B and C, the CAR dip is nearly constant until the MA, where we observe a large anomaly atop the CAR that we identify as S3. We observe that S1 is trenchward of and has shallower dip than S3 in every profile where both segments appear. S1 does not reach the MTZ while S3 does. Profile A has a shallow, flat anomaly and a discontinuous steep anomaly. We identify the shallow structure as U, the under-thrusting CAR from the north. The deep structures S3. Profile D shows a steep, fast anomaly that is preceded by gently sloping seismicity. The steep anomaly appears as twice the width of a normal slab, similar to where S1 and S3 overlap, so it could represent two slabs overlapping as proposed by Taboada et al. (2000). Profile F is an east-west dip profile that runs oblique to A–D and intersects the corner of the SdP and SM. It shows S1 and S3 with a nearly identical configuration as seen in profiles B and C. We inserted a sub-vertical anomaly for S3 into

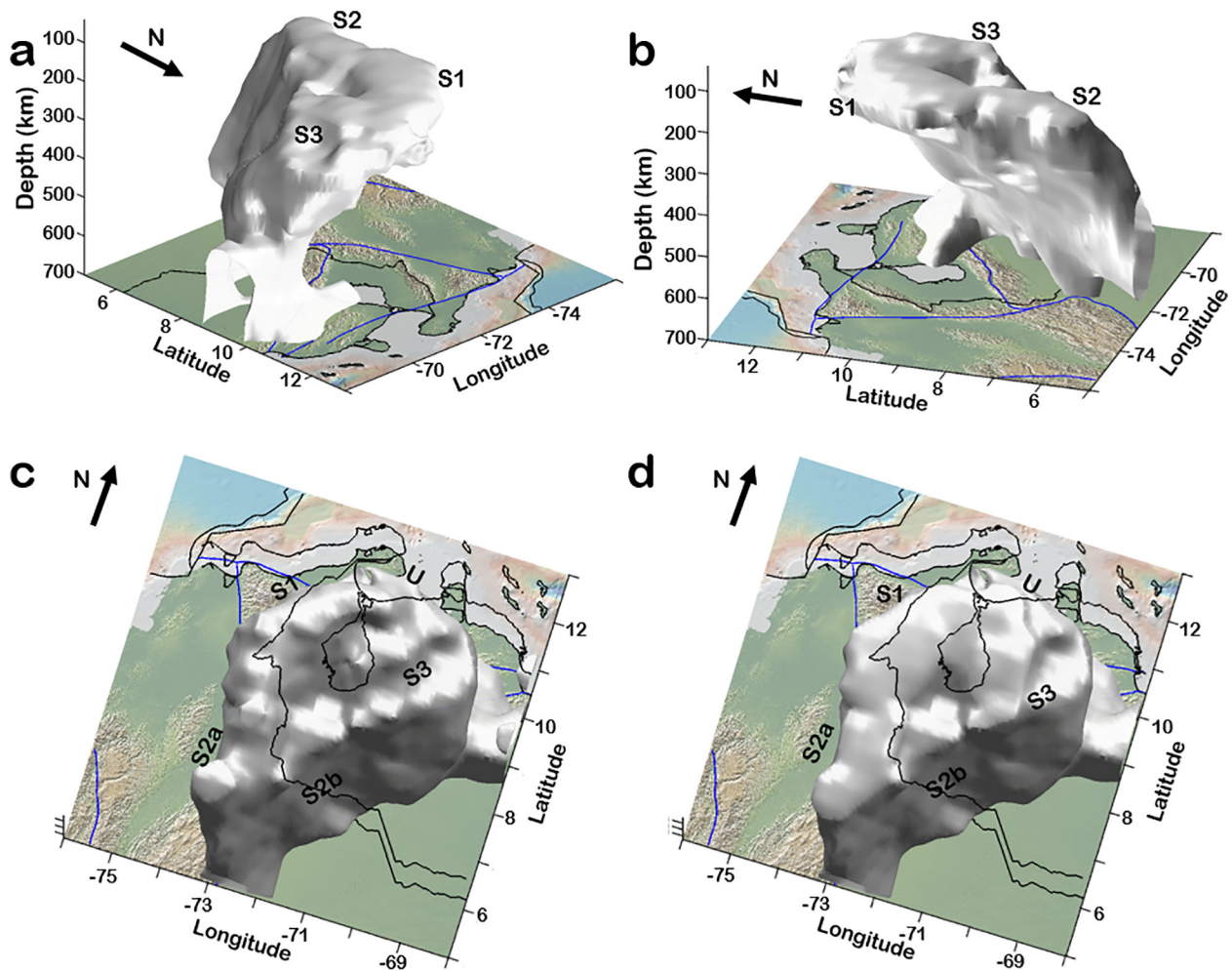


Figure 5. 3-D isosurfaces of the tomography taken at the +1.5% level. (a-b) Profile views starting at 125 km depth. (c) Map view with the surface starting at 90 km depth. In this view 2 anomlies seem possible for S2. (d) Map view with the surface starting at 160 km depth.

our synthetic and found that it was well recovered (Figure 7). The synthetic S1 was well recovered below 100 km depth across the profiles.

Profile E is nearly in the strike direction of S1 and crosses the S1 and U anomalies. A gap between the anomalies aligns with intermediate depth seismicity. We do not include a gap in the synthetic Profile E (Figure 7), and no gap is present in the recovered synthetic. Profile G runs west to east and crosses the Eastern Cordillera slightly north of the Bucaramanga nest. It shows a high amplitude, steep anomaly oriented east. Profile H traces the western margin of the MA. It shows dipping seismicity that aligns with a fast anomaly, indicating the presence of a slab. We assign the dipping anomaly to S2 while the horizontal anomaly may comprise both S1 and S3 since the profile is taken where S1 and S3 converge. Similarly, in our synthetic profile H we model a dipping S2 converging with S1 and S3 (Figure 7). All anomalies are recovered.

4. Discussion

4.1. Interpretation of the Caribbean Plate

We interpret our observations of the CAR segments as follows: U is the under-thrusting segment of the CAR that transitions to sea floor north of Venezuela and Colombia. S1 is the primary, western-most CAR slab that is currently subducting. S2 is likely part of a southern segment of the CAR, and possibly also a segment of the Nazca plate, but it is less well resolved due to array size. S2a appears in the tomography before S2b

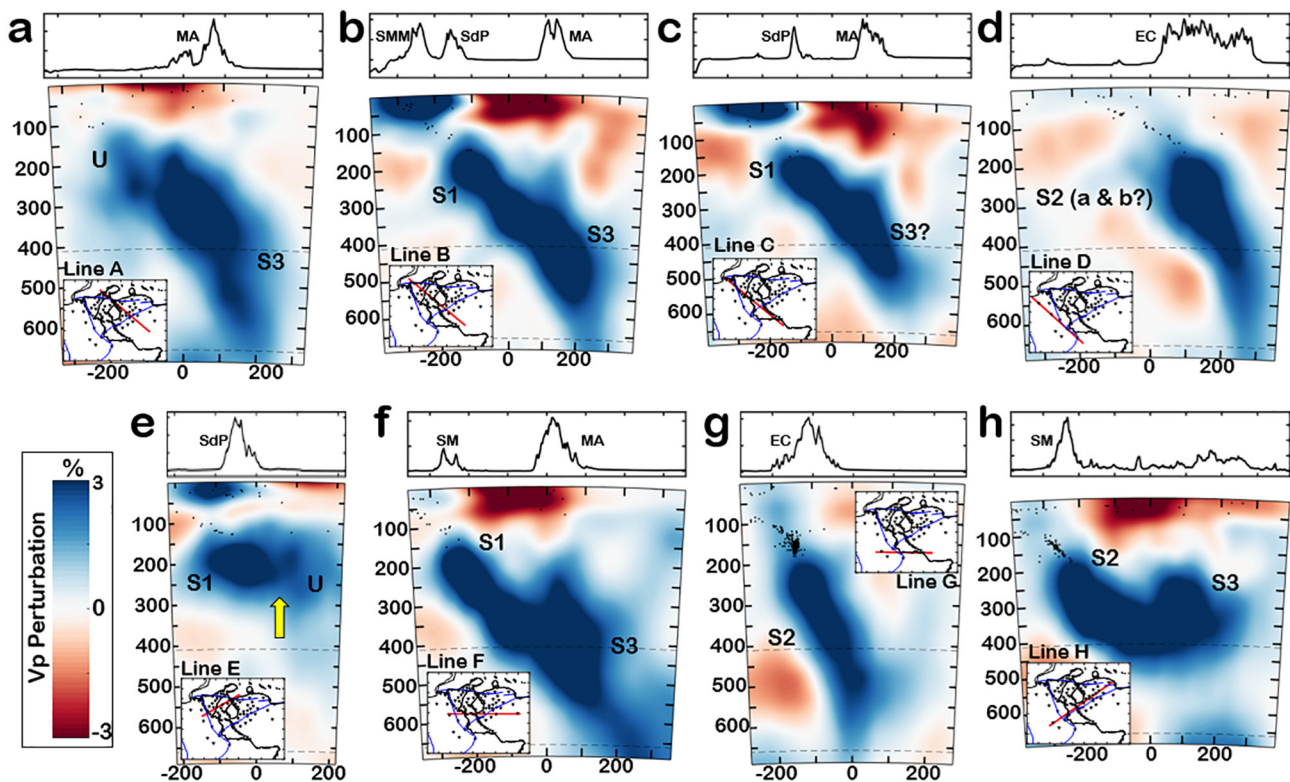


Figure 6. Cross-sections of velocity models. Black dots are seismicity as in Figure 4. S1 is the attached CAR. S2 is a southern segment possibly comprised of 2 plates. S3 is an anomaly atop the CAR we interpret as a broken segment of the CAR. Yellow arrow: Location where intermediate depth seismicity ends.

and has a north-south strike. S2b appears to have a strike similar to S1 and perhaps is connected to S1 to the northwest, outside the resolution of our study. S3 is a broken CAR segment previously attached to S1 (and possibly S2) and appears as the anomaly beneath the MA. Our interpretations are summarized as a box model in Figure 8 and surfaces in Figure S9. From these surfaces segment lengths were calculated and related to subduction timing in the following subsections.

S1 is imaged as shallow as 125 km and follows the curved curtain of seismicity along the SdP and Santander Massif at that depth. We interpret S1 as bowed concave east (Figures 4, 5 and S9). The edge of S1 coincides with the significant reduction in seismicity at intermediate depths. That site is likely the tear indicated by Mora et al. (2017), where S1 is separated from U. Figures 6a and 6b show profiles to the north and south of the proposed tear, respectively. Figure 6a lacks dipping seismicity. Figure 6b has both dipping seismicity and S1 that dips to ~400 km. Figure 6e transects the S1/U anomalies nearly along strike and shows a gap separating the anomalies where intermediate seismicity ends. We do not observe south-dipping structures originating north of the Oca-Ancón fault. Rayleigh wave tomography suggests that parts of the non-subducting Caribbean plate under-thrust northern South America south of the OAF at depths of 80 km (Miller et al., 2009). The OAF generally separates the eastward subducting S1 from the southward under-thrusting U. We estimate the length of S1 to be ~760 km.

The southern segment, S2, appears as a fast anomaly near the Bucaramanga nest. Its strike is different than the other segments at depths shallower than 230 km; it parallels seismicity along the southern Santander Massif and the Andean Eastern Cordillera. Between 310 and 530 km depth S2 appears continuous with S3 (Figure 4). Profiles D and G (Figure 6) intersect east of the BN and transect S2. Both profiles show dipping anomalies following dipping seismicity. We suggest S2a is not part of the CAR while S2b is part of the CAR, which implies that the CAR's southern boundary lies south of our study area. Many authors have proposed overlapping slabs in the Bucaramanga region (Cortes & Angelier, 2005; Prieto et al., 2012; Taboada et al., 2000; Vargas et al., 2007; Yarcé et al., 2014) but the lack of resolution along the entirety of profile D prevents us from placing the Bucaramanga nest in one plate or another. Assuming that Profile D has at least

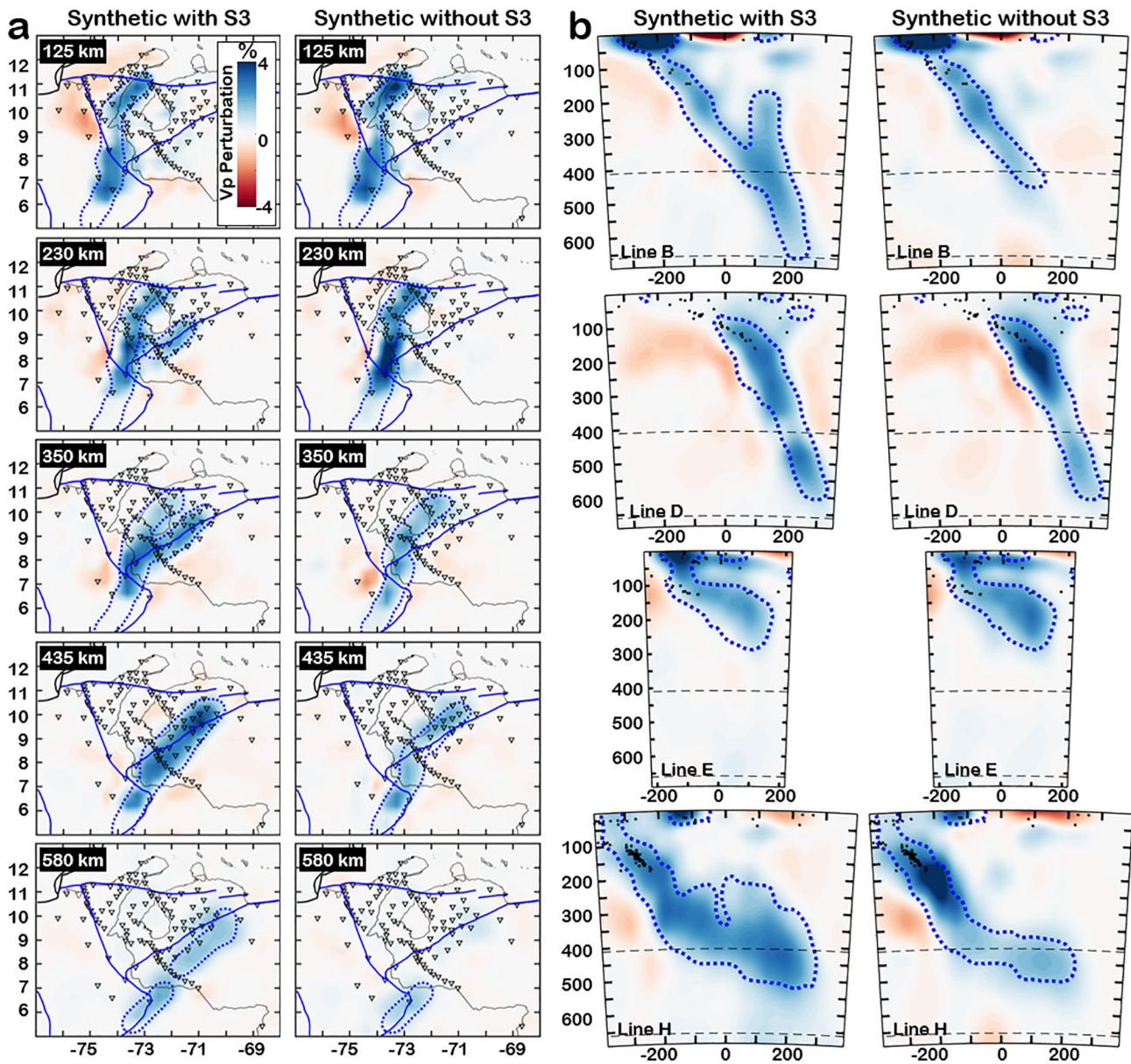


Figure 7. Synthetic image derived from surfaces in Figure S9. Dashed blue lines indicates the input model. Anomalies are the recovered image.

one slab continuous from the trench to the MTZ, we designate the entirety of that surface as S2 and estimate the length of the anomaly to be ~ 725 km. Projecting the surface back to the Caribbean Sea adds ~ 500 km for a total segment length of $\sim 1,225$ km.

The broken slab, S3, lies east of the primary slab, S1. Its apex is at ~ 160 km depth, which is ~ 175 – 225 km above the deepest tip of S1 that subducts behind it. Whether S3 penetrates the 660 transition is unclear. The upper half of S3 is nearly vertical and was likely imaged by Bezada et al. (2010). Unlike S1, the strike of S3 parallels the Mérida Andes, suggesting there was a transition in the subduction history of the CAR. We estimate the length of S3 to be ~ 450 km.

Figure 8 shows two potential geometries in the subduction system. The simplest geometry would be for S2 to comprise only the CAR (or Nazca?) (Figure 8a). In this configuration, S2 strike is parallel to the Eastern Cordillera. A challenge with this model is the discrepancy in depths where S1 and S2 meet. A more

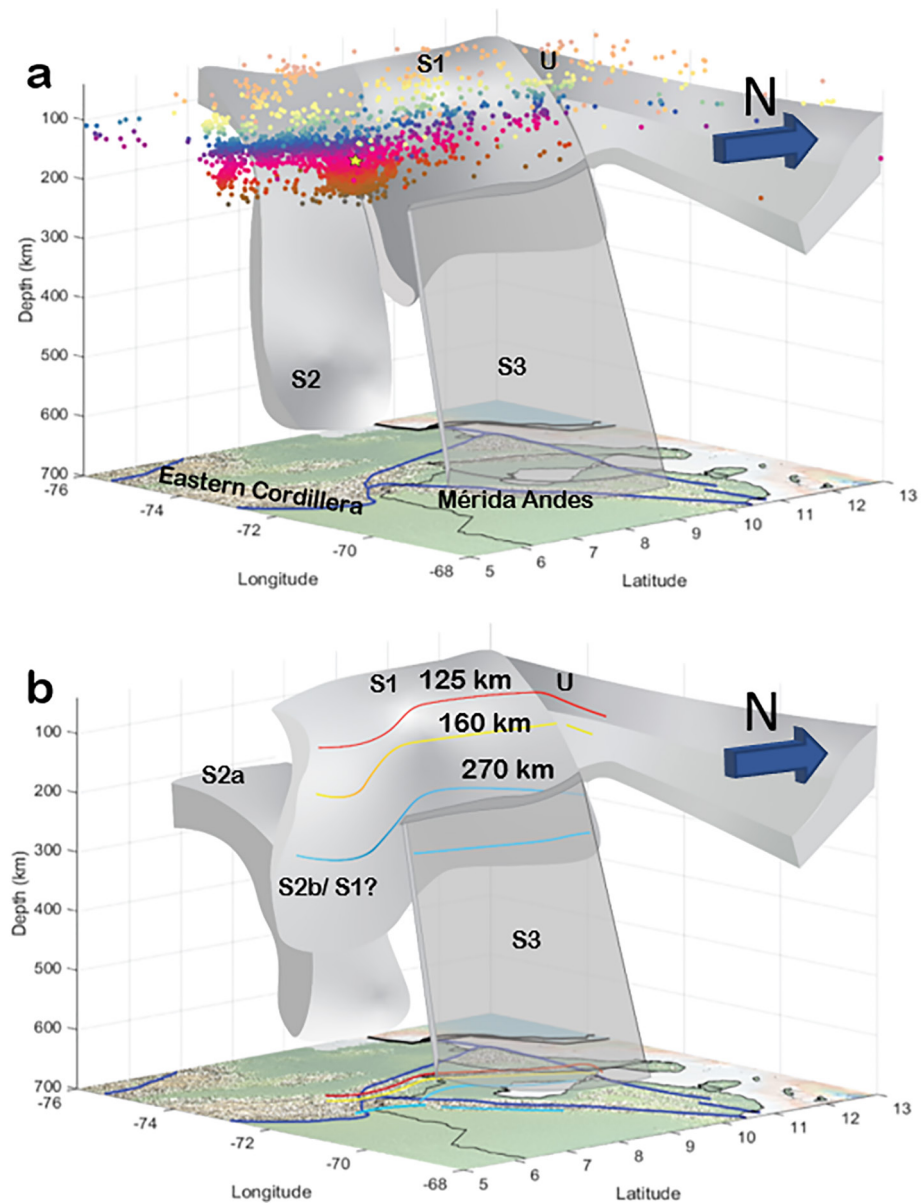


Figure 8. Box models of the Caribbean slab configuration beneath northwest South America. From the tomography, three segments were identified. (a) Model where S2 represents a single segment. (b) Model where S2 represents two segments. Lines are approximate contours lines for reference. Yellow star: Bucaramanga nest.

complicated geometry has S1 overlying S2 (Figure 8b). In this scenario S3 could only have been attached to S1 and S2b, and S2a might be the Nazca as described by Taboada et al. (2000) and Londoño et al. (2020).

4.2. Subduction History of the Caribbean Beneath NWSA

Evidence of magmatism along northwest SA dated to ~70–55 Ma indicates the normal subduction of CAR (Cardona, Valencia, Bayona, et al., 2011; Mora et al., 2017). By 45–55 Ma magmatism abruptly ceased, coinciding with major readjustment in the configuration of the South American, Caribbean, and North American Plates (Kellogg et al., 2019; Montes et al., 2019; Mora et al., 2017; Pindell et al., 1998). This magmatic cessation is interpreted as indicating the onset of low-angle subduction of the CLIP (Taboada et al., 2000). It is not clear how much of the subducted slab carries the CLIP. Assuming ~15–25 m.y. of normal subduction followed by ~45–55 m.y. of shallow subduction of CLIP at the current subduction rate of 20 mm/yr,

one could expect ~300–500 km of subducted normal crust and ~900–1,100 km of CLIP. Higher estimates of convergence rates prior to 45 Ma by Boschman et al. (2014) would increase the amount of normal CAR lithosphere subducted to 600–1,000 km, in line with estimates by Montes et al. (2019).

Our interpretation accounts for ~1,210 km of slab (S1 + S3), which falls on the lower end of the above estimate of normal crust + CLIP. Our estimates do not account for slab that might have flattened at or penetrated through the bottom of the MTZ. These estimates are greater than previous estimates by van Benthem et al. (2013), ~900 km, and Mora et al. (2017), ~1,050 km. Thus, assuming past subduction rates are close to current subduction rates, S1 accounts for ~37.5 m.y. and S3 accounts for ~22.5 m.y. for a total of ~60 m.y. of subduction. Therefore, it is likely that S3 records a history of normal subduction of the CAR. From the tomography we cannot clearly distinguish between different thicknesses of slab to determine the transition from nonCLIP to CLIP.

4.3. Breakoff of the CAR

Why, when, and where under NWSA did the CAR break? We favor a lithospheric weak point where oceanic crust transitions to CLIP as the most likely site of the break. S3, considering its length and subduction rate, carries oceanic crust and likely carries some CLIP. Dynamic models from Arrial and Billen (2013) show that change in density—due to eclogitization of a subducted plateau in their case—can ultimately lead to slab breakoff in a flat slab system. The break off occurs as the slab rolls back due to its denser tip. For the CAR this corresponds to the eclogitization of enough CLIP combined with the dense, normal slab that would have also eclogitized to provide significant density/buoyancy contrast with the remaining subducted CLIP to lead to rollback and slab detachment. While we cannot narrowly constrain the timing of the break, we rule out the buoyant CLIP entering the trench as the initiation as it would leave S3 sub-vertical in the mantle for ~45 m.y., an unlikely geometry for that length of time. Restoring S1 to its pre-break location using a sinking rate of 20 mm/yr places the breaking event under Lake Maracaibo.

The current length and position of S3 requires the slab to break no deeper than ~200 km. Eclogitization reactions may occur as shallow as 50 km in the hottest subduction zones, but the full transformation of plateau crust to eclogite will be delayed due to thicker crust and the typically cooler temperatures above a flat slab (Arrial & Billen, 2013; Gutscher et al., 2000; Hacker, 1996; Pennington, 1984). Based on a sinking rate of 20 mm/yr and the assumption that S1 began rolling back soon after the break, we propose that the midrange of possible break times is 10 Ma. A delay in rollback would require the break time to occur later while a faster sink rate would require the break to occur earlier. In the conceptual model shown in Figure 9 we back out the slab from present day to 45 Ma assuming NWSA was moving west at 20 mm/yr relative to a stationary CAR within that period. We also assume 50 km of shortening between the SdP and MA from 15 Ma to present (Monod et al., 2010). The model shows that the once-continuous slab might have been flat as far east as the eastern banks of Lake Maracaibo. That S3 is currently at least as shallow as 200 km and is positioned upright east of S1 suggests to us that breakoff initiated later in the timeline. We therefore favor a model where the slab breaks between 5 and 15 Ma.

We cannot disqualify other factors contributing to slab break off. Coeval with our proposed timeline was the Panama arc collision, which might have initiated as late as 15 Ma, influencing regional tectonics, including the North Andean orogeny (Bermúdez et al., 2010; Dengo & Covey, 1993). Far-field stresses transmitted into the region could have exploited a weakness in the CAR, leading to detachment. Vargas and Mann (2013) proposed the Panama indenter wedged its way beneath NWSA, exploiting a previous lithospheric zone of weakness leading to the Caldas tear along its southern boundary. Conceptually, they propose that the Caribbean slab is currently breaking from the Caldas tear to the Bucaramanga nest, though this tear is south of the broken slab, S3, we observe.

4.4. Implications for the Overriding Plate

As with the Rocky Mountains (Bird, 1988; English et al., 2003) and the Sierras Pampeanas (Jordan & Allmendinger, 1986; Löbens et al., 2010), flat subduction is proposed to be responsible for the uplift of SMM, SdP and MA. In Figure 10, we align our proposed timeline for CAR subduction with local and regional events. While mechanisms have been proposed to explain the uplift of the SdP and MA (Audemard &

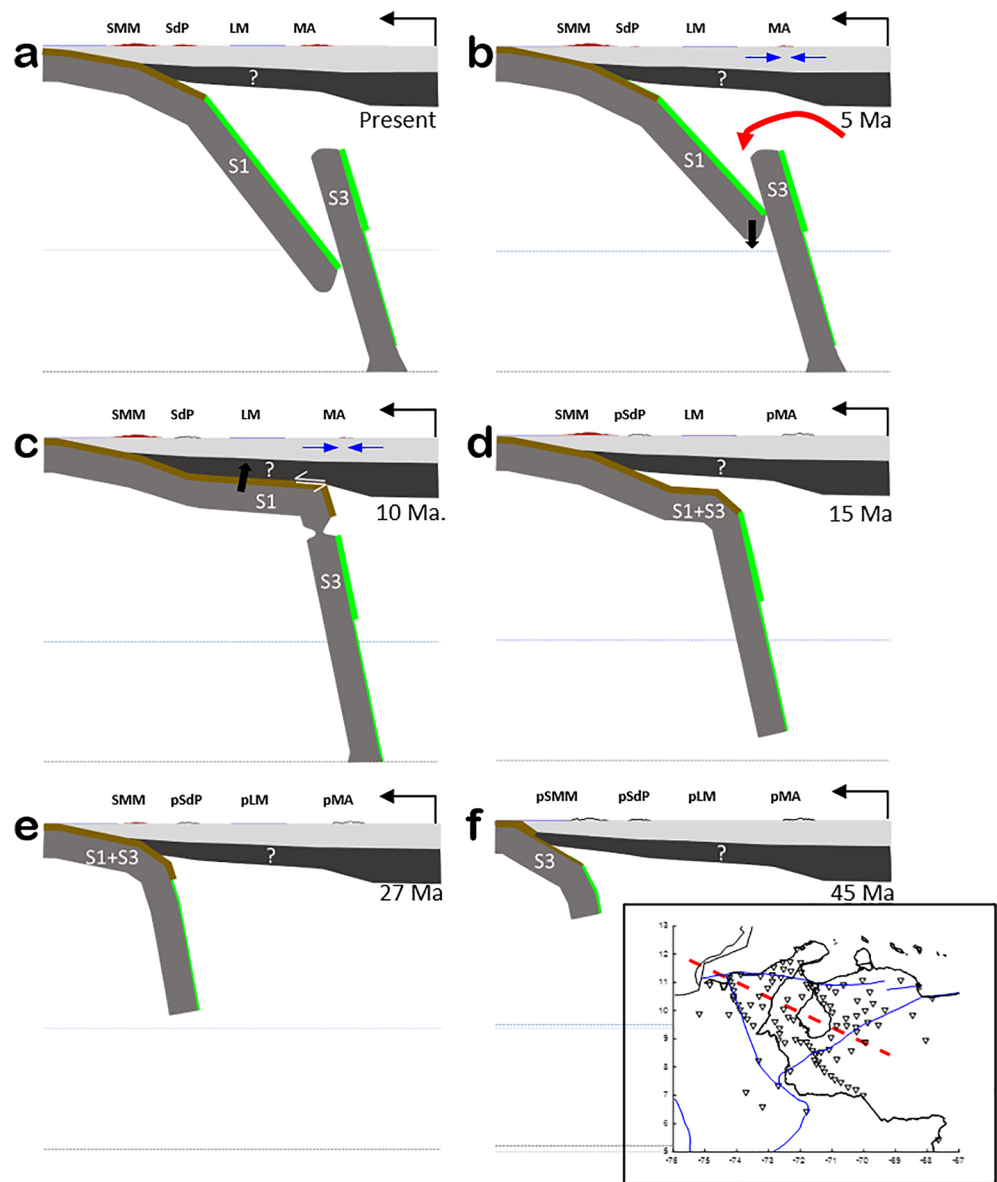


Figure 9. Conceptual sequence of slab breakup starting with present-day constraints on slab location and working backward. The CAR is stationary as SA overrides it. This model assumes a slab sinking rate of 20 mm/yr for the attached slab. Higher sinking rates allow the slab to be restored under the MA. (a) Current configuration of S1 and S3. (b) Post-break slab with S1 rollback. Red arrow indicates asthenosphere flow. Blue arrows indicate direction of tensile and compressional stresses due to asthenospheric flow induced by rollback. S3 does not sink but rotates onto S1. (c) Post-break S1 recouples with the overriding plate. S3 is pinned at the bottom of the MTZ. (d)–(f) Subduction sequence of the CAR pre-break. SMM, pSdP, pLM, and pMA mark the future locations of SMM, SdP, LM, and MA. Green and brown lines are pre-eclogitized and eclogitized crust. Thicker lines indicate CLIP. Light and dark gray are crust and mantle lithosphere, respectively. Question marks indicate our uncertainty about the state of the NWSA lithosphere.

Audemard, 2002; Colletta et al., 1997; Duerto et al., 2006; Kellogg, 1984; Monod et al., 2010), here we offer additional possible contributions to uplift due to the CAR breakoff.

The CAR currently subducts at a low angle ~50–100 km beneath SMM and ~125–175 km beneath SdP. SMM was uplifted in phases, with the most recent initiating ~ 15 Ma (Cardona, Valencia, Weber, et al., 2011). SdP was also uplifted in phases, but the main uplift occurred in the last 3 m.y., well after the arrival of the CLIP into the subduction zone (Kellogg, 1984; Kellogg & Bonini, 1982). The main uplift of the SdP coincides with the proposed timing of S1 rollback. As modeled by Buiter et al. (2001), slab roll back may induce uplift over

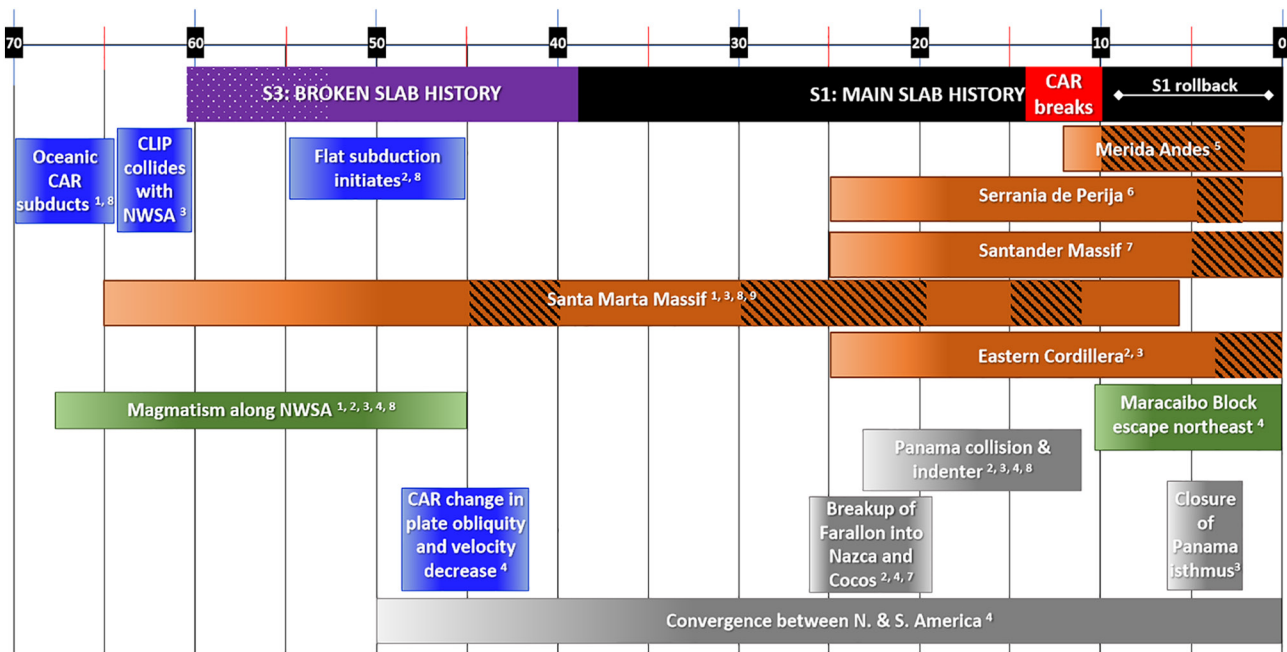


Figure 10. Timing of slabs S1 and S3 with known timings of orogenesis and other regional events. S1 and S3 lengths based on 20 mm/yr subduction rate. Length of S3 would shorten by dotted area if a 40 mm/yr rate is assumed prior to 45 Ma. The precise initiation of the Panama collision is uncertain, with dates ranging from ~22 to 12 Ma. Hatched areas indicate primary periods of uplift. (1) Cardona, Valencia, Weber, et al. (2011); (2) Taboada et al. (2000); (3) Mora et al. (2017) and references therein; (4) Boschman et al. (2014); (5) Bermudez et al. (2010); (6) Kellogg (1984); (7) Amaya et al. (2017); (8) Montes et al. (2019); (9) Cardona, Valencia, Bayona, et al. (2011).

the hinge line and this effect may be greater for a more buoyant slab—up to 4 km of uplift. The hinge line is currently under the western margin of the SdP and would have been under the eastern margin at 3 Ma. Their model also indicates a weak contribution to subsidence of a land-locked basin from rollback, which suggests a small signal of S1 rollback may be recorded in the subsidence history of the Maracaibo basin. Thus, shallow subduction of the CAR may have contributed to the initial phases of uplift of the SMM and SdP while slab rollback may have contributed to the later uplift of the SdP and subsidence of the Maracaibo basin.

How did shallow subduction of the CAR contribute to the rapid uplift of the MA? While we cannot definitively attribute the topography of the MA with slab breakoff, we consider three mechanisms that could contribute. First, the CAR remains flat beneath NWSA as far inboard as the location of the MA until S3 breaks off S1 at 10–15 m.y. ago. A sinking rate of 40 mm/yr allows S3 to be restored to the surface while still under the MA. A descent velocity of 40 mm/yr is reasonable given the plate age (Goes et al., 2011). The first contribution to the uplift of the MA is the CAR breaking into S1 and S3 and S1, with minimally eclogitized CLIP, buoyantly rising beneath the MA at ~10–12 Ma. Elastic rebound might also contribute to flattening S1 beneath NWSA. S1 would recouple with South America to transfer NW–SE directed shear stresses into the overriding plate (Figure 9c), shortening the upper plate as Jurassic-aged rift structures are reactivated (Duerto et al., 2006). A similar mechanism was proposed by Fan et al. (2014) to account for deformation during the Laramide orogeny. In their model moderate uplift was initially achieved through basal traction of the flat Farallon slab with North America that reactivated preexisting structures. A second contribution could be shear drag on the upper plate from asthenospheric flow over S3 induced by S1 rollback (Figure 9b) producing compressive stress in the overriding plate that would lead to shortening. Similarly, Fan et al. (2014) proposed that the Laramide orogeny experienced accelerated uplift when the slab rolled back due to its negative buoyancy relative to the surrounding mantle. The third contribution to the uplift of the MA is the replacement of denser oceanic lithosphere of S1 with less dense asthenospheric material, causing an isostatic response.

5. Conclusions

Our results highlight a complicated subduction system with at least three subducted CAR segments with varying strikes and dips. The main segment, S1, strikes along the seismicity under the SdP and Santander Massif. It remains flat until the Santander Massif and SdP where it dips steeply and terminates in the upper MTZ. A broken segment, S3, appears under the MA at ~160 km depth and dips steeply into the MTZ. A southern segment, S2, dips steeply under the EC and is likely flat prior to that. We assigned S2 as part of the CAR, but two seemingly distinct anomalies with different strikes suggest there might be two slabs overlapping each other. We found that we imaged ~1,210 km of slab (S1+S3), which accounts for ~60 m.y. of subduction.

The northern boundary of subduction lies south of the OAF and between the SMM and the SdP. It is marked by a gap in the tomography and a cessation of intermediate seismicity. We conclude that the southern boundary of the subducting CAR lies south of our study area.

The segmentation of the CAR opens questions of why it happened and what impact it had on the overriding plate. We hypothesize that the break between S1 and S3 occurred along a zone of lithospheric weakness or a strength contrast between CLIP and normal oceanic lithosphere. We used conceptual models to restore the CAR to a configuration just prior to break off. Depending on the sinking rate the CAR could have broken 5–15 m.y. ago. The breaking of the slab is coeval with the Panama arc collision, so it is possible the collision contributed to the break and, consequently, the uplift of the MA. The break is also coeval with the uplift of the MA. The impact of the CAR breaking on the topography of NWSA is uncertain. We hypothesize that when S3 broke from S1, S1 recoupled with the overriding plate, reactivated preexisting structures, and uplifted them. The rollback of S1 might have induced trenchward horizontal asthenospheric flow along the base of the South American lithosphere, causing northwest-directed shortening that contributed to the rapid uplift of the MA. The replacement of dense oceanic lithosphere with less dense asthenosphere may have also contributed an isostatic response in the overriding plate.

Data Availability Statement

Data collected on the CARMA array are available through the IRIS Data Management Center (https://doi.org/10.7914/SN/YU_2016). Data collected on the instruments of FUNVISIS are available by request through the agency (servicios@funvisis.gob.ve). Data collected on Servicio Geológico Colombiano instruments are freely available and accessible to the scientific community through written request and justification addressed to the Colombian Geological Survey (sismologo@sgc.gov.co).

Acknowledgments

This research was supported by the National Science Foundation under Grant No. EAR 1459047. The authors want to thank the field staff at FUNVISIS and Servicio Geológico Colombiano for their very capable operation of the CARMA seismic array. The US seismic instruments were provided by the Incorporated Research Institutions for Seismology (IRIS) through the PASSCAL Instrument Center at New Mexico Tech. At PASSCAL we thank Pnina Miller and Lloyd Carothers for field assistance and Noel Barstow for coordinating the experiment logistics. Finally, the authors thank three anonymous reviewers for their thoughtful and thorough comments that improved this manuscript. The facilities of the IRIS Consortium are supported by the National Science Foundation's Seismological Facilities for the Advancement of Geoscience (SAGE) Award under Cooperative Support Agreement EAR-1851048. Tomography color schemes were created using cbrewer (Charles, 2020).

References

- Amaya, S., Zuluaga, C. A., & Bernet, M. (2017). New fission-track age constraints on the exhumation of the Central Santander Massif: Implications for the tectonic evolution of the Northern Andes Colombia. *Lithos*, 282–283, 388–402. <https://doi.org/10.1016/j.lithos.2017.03.019>
- Antonijevic, S. K., Wagner, L. S., Kumar, A., Beck, S. L., Long, M. D., Zandt, G., et al. (2015). The role of ridges in the formation and longevity of flat slabs. *Nature*, 524(7564), 212–215. <https://doi.org/10.1038/nature14648>
- Arrial, P. A., & Billen, M. I. (2013). Influence of geometry and eclogitization on oceanic plateau subduction. *Earth and Planetary Science Letters*, 363, 34–43. <https://doi.org/10.1016/j.epsl.2012.12.011>
- Audemard, F. E., & Audemard, F. A. (2002). Structure of the Merida Andes, Venezuela: Relations with the South America-Caribbean geodynamic interaction. *Tectonophysics*, 345(1–4), 299–327. [https://doi.org/10.1016/s0040-1951\(01\)00218-9](https://doi.org/10.1016/s0040-1951(01)00218-9)
- Axen, G. J., van Wijk, J. W., & Currie, C. A. (2018). Basal continental mantle lithosphere displaced by flat-slab subduction. *Nature Geoscience*, 11, 961–964. <https://doi.org/10.1038/s41561-018-0263-9>
- Bermúdez, M. A., Kohn, B. P., van der Beek, P. A., Bernet, M., O'Sullivan, P. B., & Shagam, R. (2010). Spatial and temporal patterns of exhumation across the Venezuelan Andes: Implications for Cenozoic Caribbean geodynamics. *Tectonics*, 29(5). <https://doi.org/10.1029/2009tc002635>
- Bernal-Olaya, R., Mann, P., & Vargas, C. A. (2015). *Earthquake, tomographic, seismic reflection, and gravity evidence for a shallowly dipping subduction zone beneath the Caribbean Margin of Northwestern Colombia*. In C. Bartolini, & P. Mann (Eds.), *Petroleum geology and potential of the Colombian caribbean margin* Volume 108 (pp. 247–270). AAPG Memoir. <https://doi.org/10.1306/13531939M1083642>
- Bezada, M. J., Humphreys, E. D., Toomey, D. R., Harnafi, M., Dávila, J. M., & Gallart, J. (2013). Evidence for slab rollback in westernmost Mediterranean from improved upper mantle imaging. *Earth and Planetary Science Letters*, 368, 51–60. <https://doi.org/10.1016/j.epsl.2013.02.024>
- Bezada, M. J., Levander, A., & Schmandt, B. (2010). Subduction in the southern Caribbean: Images from finite-frequency P wave tomography. *Journal of Geophysical Research*, 115(B12). <https://doi.org/10.1029/2010JB007682>

- Bird, P. (1988). Formation of the Rocky Mountains, Western United-States: A continuum computer model. *Science*, 239(4847), 1501–1507. <https://doi.org/10.1126/science.239.4847.1501>
- Bishop, B. T., Beck, S. L., Zandt, G., Wagner, L., Long, M., Antonijevic, S. K., et al. (2017). Causes and consequences of flat-slab subduction in southern Peru. *Geosphere*, 13(5), 1392–1407. <https://doi.org/10.1130/ges01440.1>
- Boschman, L. M., van Hinsbergen, D. J. J., Torsvik, T. H., Spakman, W., & Pindell, J. L. (2014). Kinematic reconstruction of the Caribbean region since the Early Jurassic. *Earth-Science Reviews*, 138, 102–136. <https://doi.org/10.1016/j.earscirev.2014.08.007>
- Brown, W. G., Schmidt, C. J., & Perry, W. J., Jr. (1988). Deformational style of Laramide uplifts in the Wyoming foreland interaction of the Rocky Mountain foreland and the Cordilleran thrust belt. *Geological Society of America*, 171. <https://doi.org/10.1130/MEM171-p1>
- Buiter, S. J. H., Govers, R., & Wortel, M. J. R. (2001). A modeling study of vertical surface displacements at convergent plate margins. *Geophysical Journal International*, 147(2), 415–427. <https://doi.org/10.1046/j.1365-246x.2001.00545.x>
- Burke, K. (1988). Tectonic evolution of the Caribbean. *Annual Review of Earth and Planetary Science*, 16, 201–230. <https://doi.org/10.1146/annurev.ea.16.050188.001221>
- Cahill, T., & Isacks, B. L. (1992). Seismicity and shape of the subducted Nazca Plate. *Journal of Geophysical Research*, 97(B12), 17503–17529. <https://doi.org/10.1029/92JB00493>
- Cardona, A., Valencia, V. A., Bayona, G., Duque, J., Ducea, M., Gehrels, G., et al. (2011). Early-subduction-related orogeny in the northern Andes: Turonian to Eocene magmatic and provenance record in the Santa Marta Massif and Rancheria Basin, northern Colombia. *Terra Nova*, 23(1), 26–34. <https://doi.org/10.1111/j.1365-3121.2010.00979.x>
- Cardona, A., Valencia, V., Weber, M., Duque, J., Montes, C., Ojeda, G., et al. (2011). Transient Cenozoic tectonic stages in the southern margin of the Caribbean plate. *U-Th/He thermochronological constraints from Eocene plutonic rocks in the Santa Marta massif and Serranía de Jarara, northern Colombia: Geológica Acta*, 9(3–4), 445–466. <https://doi.org/10.1344/105.000001739>
- Cediel, F., Shaw, R. P., & Caacuteceres, C. (2003). Tectonic Assembly of the Northern Andean Block. In C. Bartolini, R. T. Buffler, & J. Blickwede, (Eds.), *The circum-gulf of Mexico and the Caribbean: Hydrocarbon habitats, basin formation, and plate tectonics*, American Association of Petroleum Geologists, 815–848.
- Chacín, L., Jácome, M. I., & Izarra, C. (2005). Flexural and gravity modeling of the Mérida Andes and Barinas-Apure Basin, Western Venezuela. *Tectonophysics*, 405(1), 155–167. <https://doi.org/10.1016/j.tecto.2005.06.004>
- Charles (2020). cbrewer: colorbrewer schemes for Matlab. *MATLAB Central File Exchange*. Retrieved from <https://www.mathworks.com/matlabcentral/fileexchange/34087-cbrewer-colorbrewer-schemes-for-matlab>
- Chiababba, C., De Gori, P., Faccenna, C., Speranza, F., Seccia, D., Dionicio, V., & Prieto, G. A. (2015). Subduction system and flat slab beneath the Eastern Cordillera of Colombia. *Geochemistry, Geophysics, Geosystems*, 17(1), 16–27. <https://doi.org/10.1002/2015GC006048>
- Colletta, B., Roure, F., de Toni, B., Loureiro, D., Passalacqua, H., & Gou, Y. (1997). Tectonic inheritance, crustal architecture, and contrasting structural styles in the Venezuela Andes. *Tectonics*, 16(5), 777–794. <https://doi.org/10.1029/97tc01659>
- Cortes, M., & Angelier, J. (2005). Current states of stress in the northern Andes as indicated by focal mechanisms of earthquakes. *Tectonophysics*, 403(1–4), 29–58. <https://doi.org/10.1016/j.tecto.2005.03.020>
- Dengo, C., & Covey, M. (1993). Structure of the Eastern Cordillera of Colombia: Implications for trap styles and regional tectonics. *AAPG Bulletin*, 77(8), 24. <https://doi.org/10.1306/BDF8E7A-1718-11D7-8645000102C1865D>
- De Toni, B., & Kellogg, J. (1993). Seismic evidence for blind thrusting of the northwestern flank of the Venezuelan Andes. *Tectonics*, 12(6), 1393–1409. <https://doi.org/10.1029/93tc01893>
- Duerto, L., Escalona, A., & Mann, P. (2006). Deep structure of the Mérida Andes and Serranía de Perijá mountain fronts. *AAPG Bulletin*, 90(4), 505–528. <https://doi.org/10.1306/10080505033>
- Eakin, C. M., Long, M. D., Beck, S. L., Wagner, L. S., Tavera, H., & Condori, C. (2014). Response of the mantle to flat slab evolution: Insights from local S splitting beneath Peru. *Geophysical Research Letters*, 41(10), 3438–3446. <https://doi.org/10.1002/2014GL059943>
- English, J. M., & Johnston, S. T. (2010). The Laramide Orogeny: What were the driving forces? *International Geology Review*, 46(9), 833–838. <https://doi.org/10.2747/0020-6814.46.9.833>
- English, J. M., Johnston, S. T., & Wang, K. L. (2003). Thermal modeling of the Laramide orogeny: Testing the flat-slab subduction hypothesis. *Earth and Planetary Science Letters*, 214(3–4), 619–632. [https://doi.org/10.1016/s0012-821x\(03\)00399-6](https://doi.org/10.1016/s0012-821x(03)00399-6)
- Erslev, E. A. (2005). 2D Laramide geometries and kinematics of the Rocky Mountains, Western U.S.A: Washington DC. *American Geophysical Union Geophysical Monograph Series*, 154, 7–20. <https://doi.org/10.1029/154GM02>
- Fan, M., & Carrapa, B. (2014). Late Cretaceous-early Eocene Laramide uplift, exhumation, and basin subsidence in Wyoming: Crustal responses to flat slab subduction. *Tectonics*, 33(4), 509–529. <https://doi.org/10.1002/2012tc003221>
- Goes, S., Capitanio, F. A., Morra, G., Seton, M., & Giardini, D. (2011). Signatures of downgoing plate-buoyancy driven subduction in Cenozoic plate motions. *Physics of the Earth and Planetary Interiors*, 184(1–2), 1–13. <https://doi.org/10.1016/j.pepi.2010.10.007>
- Govers, R., & Wortel, M. J. R. (2005). Lithosphere tearing at STEP faults: Response to edges of subduction zones. *Earth and Planetary Science Letters*, 236(1–2), 505–523. <https://doi.org/10.1016/j.epsl.2005.03.022>
- Guede, M., Levander, A., & Zelt, C. (2007). *Crustal structure across the Caribbean-south American plate boundary at 70W: Results from seismic refraction and reflection data*. M.S. Rice University
- Gutscher, M.-A., Malavielle, J., Lallemand, S., & Collot, J.-Y. (1999). Tectonic segmentation of the North Andean margin: Impact of the Carnegie Ridge collision. *Earth and Planetary Science Letters*, 168(3–4), 255–270. [https://doi.org/10.1016/s0012-821x\(99\)00060-6](https://doi.org/10.1016/s0012-821x(99)00060-6)
- Gutscher, M.-A., Olivet, J.-L., Aslanian, D., Eissen, J.-P., & Maury, R. (1999). The “lost Inca plateau”: Cause of flat subduction beneath Peru? *Earth and Planetary Science Letters*, 171(3), 335–341. [https://doi.org/10.1016/S0012-821X\(99\)00153-3](https://doi.org/10.1016/S0012-821X(99)00153-3)
- Gutscher, M. A., Spakman, W., Bijwaard, H., & Engdahl, E. R. (2000). Geodynamics of flat subduction: Seismicity and tomographic constraints from the Andean margin. *Tectonics*, 19(5), 814–833. [https://doi.org/10.1016/s0012-821x\(99\)00153-3](https://doi.org/10.1016/s0012-821x(99)00153-3)
- Hacker, B. R. (1996). *Eclogite formation and the rheology, buoyancy, seismicity, and H₂O content of oceanic crust*. In G. E. Bebout, D. W. Scholl, S. H. Kirby, & J. P. Platt (Eds.), *Subduction: Top to bottom*. AGU. <https://doi.org/10.1029/GM096p0337>
- Hammond, W. C., & Toomey, D. R. (2003). Seismic velocity anisotropy and heterogeneity beneath the Mantle Electromagnetic and Tomography Experiment (MELT) region of the East Pacific Rise from analysis of P and S body waves. *Journal of Geophysical Research*, 108(B4).
- Humphreys, E., Hessler, E., Dueker, K., Farmer, C. L., Erslev, E., & Atwater, T. (2003). How Laramide-age hydration of North American lithosphere by the Farallon slab controlled subsequent activity in the western United States. *International Geology Review*, 45(7), 575–595.
- Idárraga-García, J., Kendall, J.-M., & Vargas, C. A. (2016). Shear wave anisotropy in northwestern South America and its link to the Caribbean and Nazca subduction geodynamics. *Geochemistry, Geophysics, Geosystems*, 17(9), 3655–3673. <https://doi.org/10.1002/2016gc006323>
- International Seismological Centre. (2020). *On-line bulletin*. <https://doi.org/10.31905/D808B830>

- Jordan, T. E., & Allmendinger, R. W. (1986). The Sierras Pampeanas of Argentina; a modern analogue of Rocky Mountain foreland deformation. *American Journal of Science*, 286(10), 737–764. <https://doi.org/10.2475/ajs.286.10.737>
- Jordan, T. H. (1975). The present-day motions of the Caribbean Plate. *Journal of Geophysical Research*, 80(32), 4433–4439. <https://doi.org/10.1029/jb080i032p04433>
- Kay, S. M., Maksiyev, V., Moscoso, R., Mpodozis, C., & Nasi, C. (1987). Probing the evolving Andean Lithosphere: Mid-Late Tertiary magmatism in Chile (29°>–30°30'S) over the modern zone of subhorizontal subduction. *Journal of Geophysical Research*, 92(B7), 6173–6189. <https://doi.org/10.1029/jb092ib07p06173>
- Kellogg, J. N. (1984). Cenozoic tectonic history of the Serrania de-Perijá, Venezuela-Colombia, and Adjacent Basins. *Geological Society of America Memoirs*, 162, 239–261.
- Kellogg, J. N., & Bonini, W. E. (1982). Subduction of the Caribbean plate and basement uplifts in the overriding South American Plate. *Tectonics*, 1(3), 251–276. <https://doi.org/10.1029/tc001i003p00251>
- Kellogg, J. N., Camello, G. B. F., & Mora-Páez, H. (2019). Chapter 4-Cenozoic tectonic evolution of the North Andes with constraints from volcanic ages, seismic reflection, and satellite geodesy. In B. K. Horton, & A. Folguera, (Eds.), *Andean tectonics* (pp. 69–102). Elsevier.
- Kennett, B. L. N., Engdahl, E. R., & Buland, R. (1995). Constraints on seismic velocities in the Earth from traveltimes. *Geophysical Journal International*, 122, 108–124. <https://doi.org/10.1111/j.1365-246x.1995.tb03540.x>
- Kerr, A. C., Tarney, J., Marriner, G. F., Nivia, A., & Saunders, A. D. (1997). The Caribbean-Colombian cretaceous igneous province: The internal anatomy of an oceanic plateau, large igneous provinces. *Continental, Oceanic, and Planetary Flood Volcanism*, 100, 123–144.
- Levander, A. (2016). *Caribbean-Merida Andes experiment*. *International federation of digital seismograph networks*. https://doi.org/10.7914/SN/YU_2016
- Liu, L., Gurnis, M., Seton, M., Saleeby, J., Müller, R. D., & Jackson, J. M. (2010). The role of oceanic plateau subduction in the Laramide orogeny. *Nature Geoscience*, 3(5), 353–357. <https://doi.org/10.1038/ngeo829>
- Löbens, S., Bense, F. A., Wemmer, K., Dunkl, L., Costa, C. H., Layer, P., & Siegesmund, S. (2010). Exhumation and uplift of the Sierras Pampeanas: Preliminary implications from K–Ar fault gouge dating and low-T thermochronology in the Sierra de Comechingones (Argentina). *International Journal of Earth Sciences*, 100(2–3), 671–694. <https://doi.org/10.1007/s00531-010-0608-0>
- Londoño, J. M., Vallejo, K., & Quintero, S. (2020). Detailed seismic velocity structure of the Caribbean and Nazca Plates beneath Valle Medio del Magdalena region of NE Colombia. *Journal of South American Earth Sciences*, 103, 102762. <https://doi.org/10.1016/j.jsames.2020.102762>
- Malavé, G., & Suárez, G. (1995). Intermediate-depth seismicity in Northern Colombia and Western Venezuela and its relationship to Caribbean plate subduction. *Tectonics*, 14(3), 617–628. <https://doi.org/10.1029/95tc00334>
- Masy, J., Niu, F., Levander, A., & Schmitz, M. (2011). Mantle flow beneath northwestern Venezuela: Seismic evidence for a deep origin of the Mérida Andes. *Earth and Planetary Science Letters*, 305(3–4), 396–404. <https://doi.org/10.1016/j.epsl.2011.03.024>
- Masy, J., Niu, F., Levander, A., & Schmitz, M. (2015). Lithospheric expression of Cenozoic subduction, Mesozoic rifting and the Precambrian Shield in Venezuela. *Earth and Planetary Science Letters*, 410, 12–24. <https://doi.org/10.1016/j.epsl.2014.08.041>
- McQuarrie, N., & Chase, C. G. (2000). Raising the Colorado Plateau. *Geology*, 28(1), 91–94. [https://doi.org/10.1130/0091-7613\(2000\)028<0091:rtcp>2.3.co;2](https://doi.org/10.1130/0091-7613(2000)028<0091:rtcp>2.3.co;2)
- Miller, M. S., Levander, A., Niu, F., & Li, A. (2009). Upper mantle structure beneath the Caribbean-South American plate boundary from surface wave tomography. *Journal of Geophysical Research*, 114(B1). <https://doi.org/10.1029/2007jb005507>
- Monod, B., Dhont, D., & Hervouët, Y. (2010). Orogenic float of the Venezuelan Andes. *Tectonophysics*, 490(1–2), 123–135. <https://doi.org/10.1016/j.tecto.2010.04.036>
- Montes, C., Rodríguez-Corcho, A. F., Bayona, G., Hoyos, N., Zapata, S., & Cardona, A. (2019). Continental margin response to multiple arc-continent collisions: The northern Andes-Caribbean margin. *Earth-Science Reviews*, 198. <https://doi.org/10.1016/j.earscirev.2019.102903>
- Mora, J. A., Oncken, O., Le Breton, E., Ibáñez-Mejía, M., Faccenna, C., Veloza, G., et al. (2017). Linking late cretaceous to eocene tectonostratigraphy of the San Jacinto fold belt of NW Colombia with Caribbean plateau collision and flat subduction. *Tectonics*, 36(11), 2599–2629. <https://doi.org/10.1002/2017tc004612>
- Mora-Páez, H., Kellogg, J. N., Freymueller, J. T., Mencin, D., Fernandes, R. M. S., Diederix, H., et al. (2019). Crustal deformation in the northern Andes - A new GPS velocity field. *Journal of South American Earth Sciences*, 89, 76–91. <https://doi.org/10.1016/j.jsames.2018.11.002>
- Ojeda, A., & Havskov, J. (2001). Crustal structure and local seismicity in Colombia. *Journal of Seismology*, 5(4), 575–593. <https://doi.org/10.1023/A:1012053206408>
- Pennington, W. D. (1981). Subduction of the eastern Panama basin and seismotectonics of northwestern South America. *Journal of Geophysical Research*, 86(Nb11), 753–770. <https://doi.org/10.1029/jb086ib11p10753>
- Pennington, W. D. (1984). The effect of oceanic crustal structure on phase changes and subduction. *Tectonophysics*, 102(1), 377–398. [https://doi.org/10.1016/0040-1951\(84\)90023-4](https://doi.org/10.1016/0040-1951(84)90023-4)
- Pindell, J. L., Higgs, R., & Dewey, J. F. (1998). Cenozoic palinspastic reconstruction, Paleogeographic evolution and hydrocarbon setting of the Northern Margin of South America, Paleogeographic evolution and non-glacial eustasy. Northern South America. *SEPM Society for Sedimentary Geology*, 58.
- Prieto, G. A., Beroza, G. C., Barrett, S. A., López, G. A., & Florez, M. (2012). Earthquake nests as natural laboratories for the study of intermediate-depth earthquake mechanics. *Tectonophysics*, 570–571, 42–56. <https://doi.org/10.1016/j.tecto.2012.07.019>
- Ramos, V. A., & Folguera, A. (2009). *Andean flat-slab subduction through time* (Vol. 327, 1st ed., pp. 31–54). London, UK: Geological Society Publications. <https://doi.org/10.1144/SP327.3>
- Saleeby, J. (2003). Segmentation of the laramide slab-evidence from the southern Sierra Nevada region. *Geological Society of America Bulletin*, 115(6), 655–668. [https://doi.org/10.1130/0016-7606\(2003\)115<0655:sotlsf>2.0.co;2](https://doi.org/10.1130/0016-7606(2003)115<0655:sotlsf>2.0.co;2)
- Sanchez, J., Götze, H.-J., & Schmitz, M. (2010). A 3-D lithospheric model of the Caribbean-South American plate boundary. *International Journal of Earth Sciences*, 100(7), 1697–1712. <https://doi.org/10.1007/s00531-010-0600-8>
- Sanchez-Rojas, J., & Palma, M. (2014). Crustal density structure in northwestern South America derived from analysis and 3-D modeling of gravity and seismicity data. *Tectonophysics*, 634, 97–115. <https://doi.org/10.1016/j.tecto.2014.07.026>
- Schmandt, B., & Humphreys, E. (2010). Seismic heterogeneity and small-scale convection in the southern California upper mantle: Geochemistry, Geophysics. *Geosystems*, 11(5). <https://doi.org/10.1029/2010gc003042>
- Schmitz, M., Avila, J., Bezada, M., Vieira, E., Yáñez, M., Levander, A., et al. (2008). Crustal thickness variations in Venezuela from deep seismic observations. *Tectonophysics*, 459(1–4), 14–26. <https://doi.org/10.1016/j.tecto.2007.11.072>
- Servicio Geológico Colombiano. (2020). *Seismic catalog*. <http://bdrcns.sgc.gov.co/paginas1/catalogo/index.php>

- Smithson, S. B., Brewer, J., Kaufman, S., Oliver, J., & Hurich, C. (1978). Nature of the Wind River thrust, Wyoming, from COCORP deep-reflection data and from gravity data. *Geology*, 6, 648–652. [https://doi.org/10.1130/0091-7613\(1978\)6<648:notwrt>2.0.co;2](https://doi.org/10.1130/0091-7613(1978)6<648:notwrt>2.0.co;2)
- Symithe, S., Calais, E., de Chabaliere, J. B., Higgins, M., & Higgins, M. (2015). Current block motions and strain accumulation on active faults in the Caribbean. *Journal of Geophysical Research: Solid Earth*, 120(5), 3748–3774. <https://doi.org/10.1002/2014jb011779>
- Syracuse, E. M., Maceira, M., Prieto, G. A., Zhang, H., & Ammon, C. J. (2016). Multiple plates subducting beneath Colombia, as illuminated by seismicity and velocity from the joint inversion of seismic and gravity data. *Earth and Planetary Science Letters*, 444, 139–149. <https://doi.org/10.1016/j.epsl.2016.03.050>
- Taboada, A., Rivera, L. A., Fuenzalida, A., Cisternas, A., Philip, H., Bijwaard, H., et al. (2000). Geodynamics of the northern Andes: Subductions and intracontinental deformation (Colombia). *Tectonics*, 19(5), 787–813. <https://doi.org/10.1029/2000tc900004>
- Toomey, D. R., Solomon, S. C., & Purdy, G. M. (1994). Tomographic imaging of the shallow crustal structure of the East Pacific Rise at 9°30'N. *Journal of Geophysical Research*, 99(B12), 24135–24157. <https://doi.org/10.1029/94jb01942>
- van Benthem, S., Govers, R., Spakman, W., & Wortel, R. (2013). Tectonic evolution and mantle structure of the Caribbean. *Journal of Geophysical Research: Solid Earth*, 118(6), 3019–3036. <https://doi.org/10.1002/jgrb.50235>
- VanDecar, J. C., & Crosson, R. S. (1990). Determination of teleseismic relative phase arrival times using multi-channel cross-correlation and least squares. *Bulletin of the Seismological Society of America*, 80(1), 150–169.
- Van der Hilst, R. v. d., & Mann, P. (1994). Tectonic implications of tomographic images of subducted lithosphere beneath Northwestern South America. *Geology*, 22, 451–454. [https://doi.org/10.1130/0091-7613\(1994\)022<0451:tiotio>2.3.co;2](https://doi.org/10.1130/0091-7613(1994)022<0451:tiotio>2.3.co;2)
- Vargas, C. A., & Mann, P. (2013). Tearing and breaking off of subducted slabs as the result of collision of the panama arc-indenter with Northwestern South America. *Bulletin of the Seismological Society of America*, 103(3), 2025–2046. <https://doi.org/10.1785/0120120328>
- Vargas, C. A., Pujades, L. G., & Montes, L. A. (2007). Seismic structure of south-central Andes of Colombia by tomographic inversion: Geofisc. *Dermatologia Internationalis*, 46(2), 117–127.
- Yarce, J., Monsalve, G., Becker, T. W., Cardona, A., Poveda, E., Alvira, D., & Ordoñez-Carmona, O. (2014). Seismological observations in Northwestern South America: Evidence for two subduction segments, contrasting crustal thicknesses and upper mantle flow. *Tectonophysics*, 637, 57–67. <https://doi.org/10.1016/j.tecto.2014.09.006>
- Zarifi, Z., Havskov, J., & Hanyga, A. (2007). An insight into the Bucaramanga nest. *Tectonophysics*, 443(1–2), 93–105. <https://doi.org/10.1016/j.tecto.2007.06.004>

References From the Supporting Information

- Chamberlain, C. J., Hopp, C. J., Boese, C. M., Warren-Smith, E., Chambers, D., Chu, S. X., et al. (2017). EQcorrscan: Repeating and near-repeating earthquake detection and analysis in Python. *Seismological Research Letters*, 89(1), 173–181.
- Chen, C., & Holland, A. A. (2016). PhasePapy: A Robust pure Python package for automatic identification of seismic phases. *Seismological Research Letters*, 87(6). <https://doi.org/10.1785/0220160019>
- De Kool, M., Rawlinson, N., & Sambridge, M. (2006). A practical grid based method for tracking multiple refraction and reflection phases in 3D heterogeneous media. *Geophysical Journal International*, 167, 253–270.
- Eberhart-Phillips, D. (1986). Three-dimensional velocity structure in northern California Coast Ranges from inversion of local earthquake arrival times. *Bulletin of the Seismological Society of America*, 76(4), 1025–1052.
- Kissling, E., Ellsworth, W. L., Eberhart-Phillips, D., & Kradolfer, U. (1994). Initial reference models in local earthquake tomography. *Journal of Geophysical Research*, 99, 19635–19646.
- Lomax, A., Satriano, C., & Vassallo, M. (2012). Automatic picker developments and optimization: Filterpicker—a robust, broadband picker for real-time seismic monitoring and earthquake early warning. *Seismological Research Letters*, 83(3), 531–540.
- Maeda, N. (1985). A method for reading and checking phase times in autoprocesing system of seismic wave data. *Journal of the Seismological Society of Japan*, 38(2), 365–379.
- Oliphant, T. E. (2007). Python for Scientific Computing. *Computing in Science & Engineering*, 9(3), 10–20. <https://doi.org/10.1109/MCSE.2007.58>
- Panagiotakis, C., Kokinou, E., & Vallianatos, F. (2008). Automatic p-phase picking based on local-maxima distribution. *IEEE Transactions on Geoscience and Remote Sensing*, 46(8), 2280–2287.
- Rawlinson, N., de Kool, M., & Sambridge, M. (2006). Seismic wavefront tracking in 3-D heterogeneous media: applications with multiple data classes. *Exploration Geophysics*, 37, 322–330.
- Roecker, S. W., Russo, R. M., Comte, D., Carrizo, D., Peyrat, S., Opazo, T., et al. (2016). *Preliminary results from the Chile-Illapel aftershock experiment (CHILLAX)*. AGU Fall Meeting Abstracts S21B-2715.
- Sleman, R., & van Eck, T. (1999). Robust automatic p-phase picking: an on-line implementation in the analysis of broadband seismogram recordings. *Physics of the Earth and Planetary Interiors*, 113(1), 265–275.
- Waldhauser, F. (2001). HypoDD: A computer program to compute double-difference earthquake locations. *USGS Open File Report*, 01–113, 2001.
- Waldhauser, F., & Ellsworth, W. L. (2000). A double-difference earthquake location algorithm: Method and application to the northern Hayward fault. *Bulletin of the Seismological Society of America*, 90, 1353–1368.